

Dark Matter versus $h \rightarrow \gamma\gamma$ and $h \rightarrow \gamma Z$ with supersymmetric triplets

Chiara Arina¹, Víctor Martín-Lozano² and Germano Nardini^{3,4}

¹*Institut d'Astrophysique de Paris, 98bis boulevard Arago, 75014 Paris (France)*

²*Instituto de Física Teórica UAM/CSIC and Departamento de Física Teórica, Universidad Autónoma de Madrid, 28049 Madrid (Spain)*

³*Deutsches Elektronen Synchrotron, Notkestrasse 85, D-22603 Hamburg (Germany)*

⁴*Fakultät für Physik, Universität Bielefeld, D-33615 Bielefeld (Germany)*

ABSTRACT: The Triplet extension of the MSSM (TMSSM) alleviates the little hierarchy problem and provides a significant enhancement of the loop-induced diphoton rate of the lightest CP-even Higgs h . In this paper we pursue the analysis of the TMSSM Higgs phenomenology by computing for the first time the h to Z and gamma decay. Interestingly we find that the rates of loop-induced decays are correlated and their signal strengths can rise up to 40% – 60% depending on the channel. We furthermore study the dark matter phenomenology of the TMSSM. The lightest neutralino is a good dark matter candidate in two regions. The first one is related to the Higgs and Z resonances and the LSP is mostly Bino. The second one is achieved for a mass larger than 90 GeV and the LSP behaves as the well-tempered neutralino. An advantage of the triplet contribution is that the well-tempered neutralino can be a Bino-Triplino mixture, relieving the problem of achieving $M_2 \sim M_1$ in unified scenarios. The dark matter constraints strongly affect the Higgs phenomenology, reducing the potential enhancements of the diphoton and of the $Z + \text{gamma}$ channels by 20% at most. In the near future, dark matter direct searches and collider experiments will probe most of the parameter space where the neutralino is the dark matter candidate.

KEYWORDS: Phenomenology of supersymmetry, Dark Matter.

Contents

1	Introduction	1
2	The TMSSM model	4
2.1	Generic Features	4
2.2	The Higgs Mass	5
3	Higgs signatures	8
3.1	The $h \rightarrow \tilde{\chi}_1^0 \tilde{\chi}_1^0$ channel	8
3.2	The $h \rightarrow \gamma\gamma$ channel	9
3.3	The $h \rightarrow Z\gamma$ channel	10
4	Numerical analysis setup	11
5	$R_{Z\gamma}$ and $R_{\gamma\gamma}$ without DM constraints	14
6	DM phenomenology and constraints on $R_{\gamma\gamma}$ and $R_{Z\gamma}$	19
6.1	Well-tempered ‘Bino-Triplino’ neutralino	20
6.2	DM at the Higgs and Z resonances	21
6.3	DM in the TMSSM: global survey	24
6.4	DM implications on $R_{\gamma\gamma}$ and $R_{Z\gamma}$	26
7	Conclusions	28

1 Introduction

The discovery of the Higgs boson [1, 2] has closed a long era: its mass is no more a free parameter. Its value $m_h \simeq 126$ GeV is in agreement with the mass range predicted in supersymmetric scenarios [3]. Nevertheless, the minimal version of these models, the so-called Minimal Supersymmetric Standard Model (MSSM), turns out to be ailing by the LHC discovery. The value $m_h \simeq 126$ GeV is indeed well above the one that the MSSM *naturally* predicts, and heavy third generation squarks and large stop mixing are required to reproduce the measured mass [4–7]. The MSSM electroweak sector therefore needs an unpleasant amount of fine tuning and a little hierarchy problem plagues the model.

In non-minimal supersymmetric scenarios this problem can be alleviated. They can indeed involve new contributions (absent in the MSSM) that rise the tree-level prediction of the Higgs mass. For this reason smaller radiative corrections and less tuning in the electroweak sector are required. The drawback of this important achievement is (partial) loss of predictivity since extra free parameters have been introduced. A compromise between

naturalness and predictivity is thus to consider scenarios extending the MSSM as little as possible.

If one does not enlarge the gauge symmetry group of the Standard Model (SM), the only extension boosting the tree-level Higgs mass is to couple new chiral superfields to the Higgs sector of the superpotential. To this aim only singlets and $SU(2)_L$ triplets with hypercharges $Y = 0, \pm 1$ are allowed by gauge invariance [8]. Whereas the former option has been deeply studied, see e.g. [9] and references therein, the latter is less known and has received special attention only after ATLAS and CMS initially measured sizeable deviations in the diphoton Higgs rate [10, 11]. Indeed, the triplet superfield involves extra charginos that can largely enhance the diphoton channel [12–14] without requiring peculiar features such as large deviations in the main Higgs decay rates, huge stop masses, ultra light charginos or very heavy Higgsinos as it occurs in other scenarios [5, 15–17]. In particular, such an enhancement can be achieved in both decoupling and non-decoupling regime (i.e. with large and small CP-odd Higgs mass m_A) while resembling the dominant SM Higgs couplings [18].

Although the observed Higgs signal strengths [1, 2] might appear SM-like because of an accidental compensation between production and decay rates that per se differ from the SM predictions, it is still worth to analyze scenarios where each Higgs decay but the loop-induced ones, and Higgs production is SM-like. In this simplified approach, indeed, it is easier to highlight the origin of a potential deviation (in loop-induced channels) that lies on the top of the global suppression/enhancement present in all channels. Such a deviation is somehow expected since loop-induced processes are particularly sensitive to new physics that can not perturb the dominant Higgs channels. This method has been applied in ref. [12] to show that charginos can provide up to 45% diphoton enhancement in the $Y = 0$ Triplet extension of the MSSM (TMSSM).

The same approach is applied in the present paper. We extend the analysis of ref. [12] to a broader parameter space and we find that a slightly larger enhancement of about 60% can be achieved via chargino contributions. More interestingly, we show that this departure from the SM prediction is tightly correlated to the deviation in the $h \rightarrow Z\gamma$ channel. In any case, the $\Gamma(h \rightarrow Z\gamma)$ rate can never be larger than about 1.4 times its SM value ¹.

These upper bounds are obtained without imposing any Dark Matter (DM) constraint on the TMSSM field content. Nevertheless they are compatible with the DM observables if the Higgs phenomenology is somehow disentangled from the DM puzzle. This is achieved for instance by invoking gravitinos, axions and axinos as DM candidates [20–23], or by postulating cosmological scenarios with non-standard DM production [24]. On the contrary, if the DM candidate is required to be the Lightest Supersymmetric Particle (LSP) of the TMSSM within the traditional cosmological assumptions, the above bounds should be revisited. To this aim we pursue the analysis of the Higgs phenomenology for the case having the lightest neutralino as DM particle. In order to capture the most stringent features related to the $h \rightarrow Z\gamma$ and $h \rightarrow \gamma\gamma$ enhancements, we require the relic density to rely only on the chargino, neutralino and SM fields. In other words, besides analyzing

¹For studies on the $Z\gamma$ channel in other non-minimal supersymmetric frameworks see i.e. refs. [17, 19].

the DM annihilation via Higgs and Z boson resonances, we study a kind of well-tempered neutralino in the TMSSM.

By definition the well-tempered neutralino in the MSSM is a tuned mixture of gaugino and Higgsino that achieves the correct relic density away from resonances and coannihilations with other supersymmetric particles [25]. The successful parameter space consists of either the Bino and Higgsinos, or the Bino and Wino having almost degenerate mass terms. Other issues however jeopardize these two scenarios: the former is strongly constrained by limits on the DM Spin-Independent (SI) elastic scattering, and the latter seems unnatural since supersymmetry breaking mechanisms unlikely lead to degenerate Bino and Wino soft masses.

Introducing the TMSSM fermionic triplet, hereafter dubbed Triplino, provides new features to the DM phenomenology. In fact, the Triplino can play the role of the Wino component, making the tuning between Bino, Wino and Higgsinos masses unnecessary and opening up a new viable DM parameter space for the well-tempered neutralino. Moreover, the Triplino mass parameter is a superpotential term that in principle can be produced by supersymmetry breaking sources different from those generating the gaugino masses ².

Interestingly, we find that in the TMSSM the DM constraints strongly impact the loop-induced Higgs processes. Independently on the regions where the LSP achieves the observed relic density the $h \rightarrow \gamma\gamma$ and $h \rightarrow Z\gamma$ enhancements cannot be larger than 20%. This mostly occurs because larger enhancements need light Higgsino and Triplino mass parameters, which tend to push the SI elastic scattering off nuclei of the lightest neutralino above the LUX exclusion limit [26].

The rest of the paper is organized as follows. In section 2 we review the basic features of the TMSSM and its most natural parameter space. We also present some improvements in the determination of the lightest Higgs mass m_h . Section 3 describes the Higgs signatures in the TMSSM, with emphasis to the Higgs invisible width and loop-induced decay channels. In particular, the first calculation of the $\Gamma(h \rightarrow Z\gamma)$ width in the TMSSM is presented here. Section 4 is dedicated to set up the method of our numerical analysis, as well as the parameter choice. Section 5 studies in detail the signal strengths of loop-induced Higgs decays and their correlation. We then move to discuss the DM phenomenology and its impact on the Higgs signatures in section 6. Section 7 is finally devoted to summarize our findings.

²For instance, one can produce the gaugino masses via gauge mediation and the mass parameters of Higgsinos and Triplinos via the Giudice-Masiero mechanism. Notice that the TMSSM does not seem to be in tension with gauge mediation due to the Higgs mass $m_h \approx 126$. Indeed, no large trilinear parameters are required to naturally achieve the observed Higgs mass [12].

2 The TMSSM model

2.1 Generic Features

In the TMSSM the matter content of the MSSM is extended by a $Y = 0$ $SU(2)_L$ -triplet superfield

$$\Sigma = \begin{pmatrix} \xi^0/\sqrt{2} & \xi_2^+ \\ \xi_1^- & -\xi^0/\sqrt{2} \end{pmatrix}. \quad (2.1)$$

In comparison with the MSSM, the TMSSM superpotential and soft-breaking Lagrangian contain respectively two and three extra renormalizable terms [8, 27]:

$$W_{\text{TMSSM}} = W_{\text{MSSM}} + \lambda H_1 \cdot \Sigma H_2 + \frac{1}{2} \mu_\Sigma \text{Tr} \Sigma^2, \quad (2.2)$$

$$\mathcal{L}_{\text{TMSSM}_{\text{SB}}} = \mathcal{L}_{\text{MSSM}_{\text{SB}}} + m_4^2 \text{Tr}(\Sigma^\dagger \Sigma) + [B_\Sigma \text{Tr}(\Sigma^2) + \lambda A_\lambda H_1 \cdot \Sigma H_2 + \text{h.c.}] , \quad (2.3)$$

where $A \cdot B \equiv \epsilon_{ij} A^i B^j$ with $\epsilon_{21} = -\epsilon_{12} = 1$ and $\epsilon_{22} = \epsilon_{11} = 0$. For sake of simplicity we assume no sources of CP violation and consequently all parameters are taken as real.

In general the neutral scalar component ξ^0 acquires a VEV $\langle \xi^0 \rangle$. Electroweak precision observables impose $\langle \xi^0 \rangle \lesssim 4 \text{ GeV}$ at 95% CL [18, 28] which, unless of a tuning on the parameters, corresponds to the hierarchy

$$|A_\lambda|, |\mu|, |\mu_\Sigma| \lesssim 10^{-2} \frac{m_\Sigma^2 + \lambda^2 v^2/2}{\lambda v}, \quad (2.4)$$

with $m_\Sigma^2 \equiv m_4^2 + \mu_\Sigma^2 + B_\Sigma \mu_\Sigma$. For A_λ , μ and μ_Σ at the electroweak scale, such a hierarchy requires $m_\Sigma \gtrsim 2 \text{ TeV}$ [18]³. As a consequence, the mixing between the MSSM Higgs sector and the scalar triplet is rather small and it can be safely neglected for $m_\Sigma \gtrsim 5 \text{ TeV}$ [12]. These values of m_Σ as well as the hierarchy in eq. (2.4) will be assumed in the following. This in particular allows to take $\langle \xi^0 \rangle \approx 0$.

As the Σ scalar components decouple from the Higgs fields H_1 and H_2 , which interact with the down and up right-handed quarks respectively, the Higgs sector at the electroweak scale looks like the one of the MSSM with some $\mathcal{O}(\lambda^2 v^2)$ shifts in the tree-level mass spectrum. By imposing the minimization conditions for the electroweak symmetry breaking, it turns out [18]

$$m_3^2 = m_A^2 \sin \beta \cos \beta, \quad (2.5)$$

$$m_Z^2 = \frac{m_2^2 - m_1^2}{\cos 2\beta} - m_A^2 + \lambda^2 v^2/2, \quad (2.6)$$

$$m_A^2 = m_1^2 + m_2^2 + 2|\mu|^2 + \lambda^2 v^2/2, \quad (2.7)$$

$$m_H^\pm = m_A^2 + m_W^2 + \lambda^2 v^2/2, \quad (2.8)$$

where $\tan \beta = v_2/v_1$, $v = \sqrt{v_1^2 + v_2^2} = 174 \text{ GeV}$, m_Z and m_W are the Z and W vector boson masses, and m_1^2 , m_2^2 and m_3^2 are the usual MSSM soft parameters of the Higgs fields

³For discussions on the naturalness of such a hierarchical scenario see refs. [12, 18].

$H_{1,2}$ whose neutral components are decomposed as $H_i^0 = v_i + (h_i + i\chi_i)/\sqrt{2}$. Moreover, the CP-even squared mass matrix in the basis (h_2, h_1) is given by

$$\mathcal{M}_{h,H}^2 = \begin{pmatrix} m_A^2 \cos^2 \beta + m_Z^2 \sin^2 \beta & (\lambda^2 v^2 - m_A^2 - m_Z^2) \sin \beta \cos \beta \\ (\lambda^2 v^2 - m_A^2 - m_Z^2) \sin \beta \cos \beta & m_A^2 \sin^2 \beta + m_Z^2 \cos^2 \beta \end{pmatrix}. \quad (2.9)$$

The contributions $\mathcal{O}(\lambda^2 v^2)$ lift the lightest eigenvalue m_h^2 and the little hierarchy problem can be then alleviated with respect to the MSSM. This can be easily seen in the limit $m_A \rightarrow \infty$ where

$$m_{h,tree}^2 = m_Z^2 \cos^2 2\beta + \frac{\lambda^2}{2} v^2 \sin^2 2\beta. \quad (2.10)$$

The $\mathcal{O}(\lambda^2 v^2)$ term can provide a sizeable boost to m_h . In particular, no large radiative corrections are required to catch $m_h \simeq 126$ GeV for large λ and small $\tan \beta$ ⁴.

On the other hand, some rather large radiative corrections to the Higgs sector are unavoidable due to the lack of experimental evidence of stops and gluinos. Within the specific assumptions the experimental analyses are based on [29], stop and gluino bounds in the presence of any lightest neutralino mass are quite stringent, namely $m_{\tilde{t}} \gtrsim 650$ GeV and $M_3 \gtrsim 1.4$ TeV [30–32] (for loopholes see e.g. refs. [33, 34]). Their radiative corrections to the Higgs sector are then sizeable and need to be stabilized at the expense of a certain amount of fine tuning in the model (for details see e.g. ref. [35]).

A further important source of tuning comes from the triplet if m_Σ is large. We require this to be subdominant to the gluino and stop ones in order to alleviate the little hierarchy problem as much as possible. Notice that this condition does not prevent from $m_\Sigma > m_{\tilde{t}}$ since triplets have less degrees of freedom and (typically) smaller coupling to $H_{u,d}$ than stops. In this respect, the parameter choice $m_\Sigma \gtrsim 5$ TeV, $m_{\tilde{t}} \gtrsim 650$ GeV and $\lambda \lesssim 1$ is allowed [12, 18].

In order to simplify our analysis, we will restrict the parameter space to a subset where all the above issues are taken into account. We will focus on the parameter region

$$m_\Sigma = 5 \text{ TeV}, \quad A_t = A_b = 0, \quad M_3 = 1.4 \text{ TeV}, \quad m_A = 1.5 \text{ TeV}, \quad (2.11)$$

$$\lambda \lesssim 1, \quad \tan \beta \sim \mathcal{O}(1), \quad \tilde{m} \gtrsim 750 \text{ GeV}, \quad (2.12)$$

with $\tilde{m} = m_U = m_D = m_Q$. This choice indeed (i) alleviates the little hierarchy problem as it boosts m_h with subdominant Σ radiative corrections. Moreover, as far as μ_Σ and μ are not too large, it (ii) naturally satisfies the hierarchy (2.4) and (iii) allows to neglect the mixing between the Σ scalars and the low energy sector. All sleptons are considered heavy enough not to interact with the relevant SUSY spectrum; numerically they have been taken to be 3 TeV. The precise parameter space we consider is defined in section 4, together with all observational constraints used in this analysis.

2.2 The Higgs Mass

Nowadays the LHC measurement of the Higgs mass is very accurate. The most recent analyses present 2- σ uncertainties of about 1% on the central value $m_h \simeq 125.6$ GeV [1, 36].

⁴Nevertheless, large values of λ generate a Landau pole and the TMSSM may require an ultraviolet completion to maintain perturbativity up to the unification scale.

Such accuracy goes much further than the typical precision that beyond-the-SM theoretical papers achieve. These works indeed are more aimed to capture the qualitative features of new frameworks than to accurately evaluate their predictions.

In this spirit, seminal works on the TMSSM have analyzed the Higgs sector at tree-level approximation [3, 8, 27]. Dominant one-loop corrections coming from stops and scalar triplets, as well as one-loop contributions from heavy Higgsinos and Triplinos, have been included only recently [12, 18, 37]. Despite these efforts, the theoretical uncertainties on the TMSSM Higgs mass spectrum is far from being comparable with the experimental one.

A pragmatic approach to this problem is to absorb the (potentially large) theoretical error on m_h into an effective uncertainty on the high energy parameters, especially on the m_U , m_Q and m_Σ soft-breaking terms (and on the trilinear parameters if they are allowed to be large). It is however problematic to quantify the latter uncertainty and how it propagates to the physical observables. For instance, big effects can arise in the DM relic density in the neutralino-stop coannihilation region, or in the SI cross-section when stop mediation dominates the interaction. On the other hand, less dramatic effects arise when the parameters absorbing the Higgs theoretical uncertainty provide sub-leading corrections to the observables. In order to reduce these uncertainties, here we improve the recent TMSSM Higgs mass calculations [12, 18, 37] and consider loop effects in the whole mass spectrum.

For this purpose we use the SARAH-3.3.0 program [38, 39] to obtain the full two-loop Renormalization Group Equations (RGEs). The code, which works in the $\overline{\text{DR}}$ renormalization scheme, also provides the full one-loop ElectroWeak-Symmetry Breaking (EWSB) conditions and full one-loop spectrum to which we include some $\mathcal{O}(h_t^2 g_3^2)$ and $\mathcal{O}(h_t^4)$ two-loop contributions.

The RGEs are solved numerically by the SPheno-3.2.4 [40, 41] code. The solution fulfills the above EWSB conditions at the electroweak scale m_Z , as well as some experimental constraints (e.g. the quark mass spectrum; for details see refs. [40, 41]). It is univocally determined once we choose the values of the residual free parameters of the theory⁵. These inputs are given (and we will quote them) at the SUSY renormalization scale, Q .

Once the RGEs are solved, all running parameters and couplings at the scale Q are known. These are used to determine the pole mass spectrum. In this way, we determine the pole mass m_h at full one-loop plus $\mathcal{O}(h_t^2 g_3^2) + \mathcal{O}(h_t^4)$ two-loop order on top of the two-loop RGE resummation⁶.

The renormalization scale dependence $m_h(Q)$ highlights the improvement in the Higgs mass calculation and it is presented in figure 1 for several values of λ and the parameter setting in eq. (2.11) with $\mu_\Sigma = M_1 = 150$ GeV. In the figure solid (dotted) [dotted-dotted-dashed] lines are plotted for $\tilde{m} = 700$ GeV and $\mu = M_2 = 300$ GeV ($\tilde{m} = 700$ GeV and

⁵The quantities M_1^2 , M_2^2 and A_λ are fixed as functions of the other parameters through the EWSB equations with $B_\Sigma = 0$.

⁶We include the $\mathcal{O}(h_t^2 g_3^2)$ and $\mathcal{O}(h_t^4)$ two-loop effects since we expect $\mathcal{O}(h_t^2 \lambda^2)$ corrections to be subdominant in the regime $\lambda \lesssim 1$ and small $\tan \beta$ due to the color factors and $h_t^2 = m_t^2 / \sin^2 \beta \lesssim \lambda^2$. These $\mathcal{O}(h_t^2 g_3^2)$ and $\mathcal{O}(h_t^4)$ corrections match with those of the MSSM and are therefore easy to implement in SPheno (for details see ref. [42] and references therein).

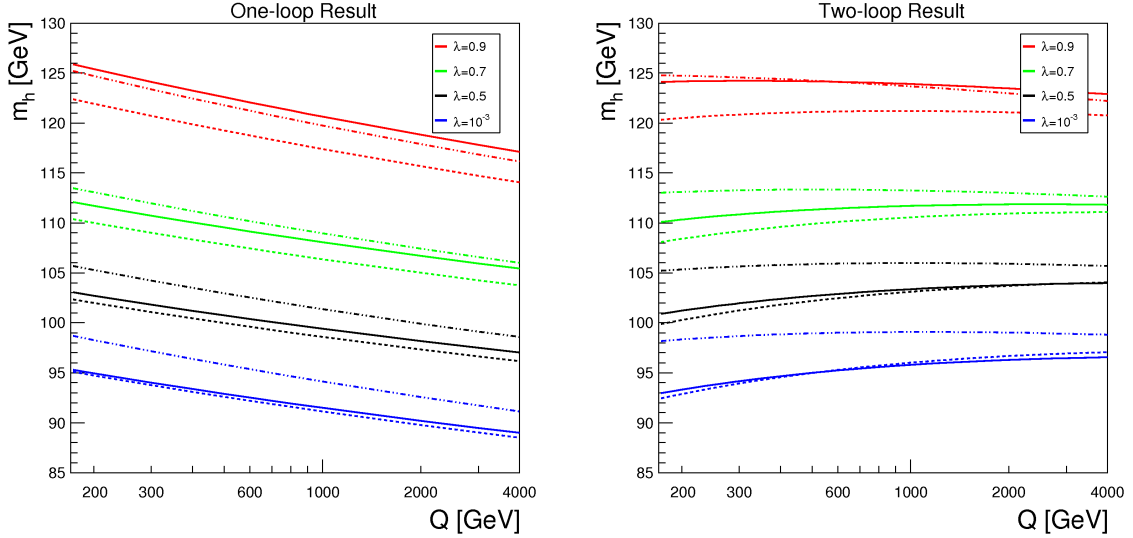


Figure 1. *Left:* The Higgs mass m_h as a function of the SUSY renormalization scale Q in the one-loop approximation. *Right:* Same as left in the two-loop approximation. Same color identifies same input value of λ , as labelled. A subset of parameters is fixed at: $\mu_\Sigma = M_1 = 150$ GeV, $m_A = 1.5$ TeV, $m_\Sigma = 5$ TeV, $A_t = A_b = 0$ and $M_3 = 1.4$ TeV. Solid lines (dashed lines) [dotted-dotted-dashed lines] are evaluated for $\tilde{m} = 700$ GeV and $\mu = M_2 = 300$ GeV ($\tilde{m} = 700$ GeV and $\mu = M_2 = 1$ TeV) [$\tilde{m} = \mu = M_2 = 1$ TeV].

$\mu = M_2 = 1$ TeV) [$\tilde{m} = \mu = M_2 = 1$ TeV]. The scale dependence is strongly reduced by going from one-loop (left panel) to two-loop (right panel) order. The addition of the $\mathcal{O}(h_t^2 g_3^2) + \mathcal{O}(h_t^4)$ contributions is then crucial to improve the result, as it is well known in the MSSM ⁷ (cf. curves at $\lambda = 10^{-3}$), whereas the undetermined $\mathcal{O}(\lambda^2 h_t^2)$ corrections seem to be subdominant even at $\lambda \approx 1$.

Figure 1 also guides in the choice of Q . The $\mathcal{O}(h_t^2 g_3^2) + \mathcal{O}(h_t^4)$ corrections are minimized at Q nearby the electroweak scale, and $m_h(Q \approx m_t)$ is then expected to be quite stable under further radiative corrections. Although the exact number slightly depends on the parameter choice, for concreteness we fix $Q = m_t$ in the rest of the analysis.

A last comment concerns the chargino and neutralino parameters. As shown in the figure, if (part of) the chargino spectrum is heavy, relevant negative corrections to m_h can arise [37]. For instance, depending on the value of λ , m_h is lowered by about 1÷4 GeV by moving $\mu = M_2$ from 300 GeV to 1 TeV when $\tilde{m} = 700$ GeV and $\mu_\Sigma = M_1 = 150$ GeV (c.f. dotted and solid curves of figure 1). Of course, this decrement can be compensated by modifying either $(\lambda, \tan \beta)$ and/or by increasing \tilde{m} , as the dotted-dotted-dashed lines highlight.

⁷Notice that the lines with very small λ reproduce the MSSM result except of modifications due to the extra $SU(2)_L$ -charged content provided by the triplet.

3 Higgs signatures

Since our aim is to explore the qualitative capabilities of the TMSSM, in particular those related to DM features, we do not look for interplay of Higgs production and decay widths to overcome the LHC bounds. We instead try to work well within the ballpark allowed by data, that is, we attempt to reproduce a SM-like Higgs sector.

The first step in this direction is to fix the tree-level Higgs couplings to SM fields. They are SM-like if, on the top of our assumption $m_\Sigma \gg m_h$, it occurs either (i) m_A is much larger than m_h or (ii) $\tan\beta$ and λ have values within the so-called alignment region [18]. Here we focus on the first possibility. In this case results are independent of the specific choice of m_A and we can thus fix $m_A = 1.5 \text{ TeV}$ without lack of generality.

The second step is to check the radiative corrections to the Higgs couplings coming from non-SM particles. For our parameter choice, given in eqs. (2.11) and (2.12), loop corrections to tree-level interactions are negligible. They may instead be responsible of important deviations from the SM in loop-induced processes. For gluon fusion, which is the main Higgs production mechanism at LHC, no relevant deviation arises in our analysis since squarks are assumed rather heavy and $\tan\beta$ is small. Therefore, the total Higgs production is SM-like. On the contrary, charginos may be light and eventually the $\Gamma(h \rightarrow \gamma\gamma)$ and $\Gamma(h \rightarrow Z\gamma)$ widths may depart from their SM values. However, these two processes are not yet well measured due to lack of statistics and of indirect impact on other processes: in practice $\Gamma(h \rightarrow \gamma\gamma)$ and $\Gamma(h \rightarrow Z\gamma)$ are so small that they play no role in the branching ratios of other Higgs decays. For this reason we do not force them to be SM-like, as we aim to do with the dominant Higgs channels.

Finally, one has to guarantee that no new relevant Higgs decay process is open. This typically occurs when the mass of the lightest neutralino is sufficiently small to allow for the $h \rightarrow \tilde{\chi}_1^0 \tilde{\chi}_1^0$ channel. In such a case, any signal strength $R_{XY} \equiv \text{BR}(h \rightarrow XY)/\text{BR}_{\text{SM}}(h \rightarrow XY)$ calculated by disregarding the invisible width, should be corrected by the factor $1 - \text{BR}(h \rightarrow \tilde{\chi}^0 \tilde{\chi}^0)$ ⁸. As the branching ratio $\text{BR}(h \rightarrow \tilde{\chi}^0 \tilde{\chi}^0)$ is bounded by ATLAS and CMS analyses [43, 44], it is worth to estimate it.

3.1 The $h \rightarrow \tilde{\chi}_1^0 \tilde{\chi}_1^0$ channel

The Higgs decay channel into a pair of lightest neutralinos is open for $m_{\tilde{\chi}_1^0} < m_h/2$. Its width is given by

$$\Gamma(h \rightarrow \tilde{\chi}_1^0 \tilde{\chi}_1^0) = \frac{G_F m_W^2}{2\sqrt{2}\pi} m_h \left(1 - \frac{4m_{\tilde{\chi}_1^0}^2}{m_h^2}\right)^{3/2} g_{h\tilde{\chi}_1^0\tilde{\chi}_1^0}^2, \quad (3.1)$$

where

$$g_{h\tilde{\chi}_1^0\tilde{\chi}_1^0} = (N_{12} - \frac{g_1}{g_2} N_{11})(\sin\beta N_{14} - \cos\beta N_{13}) + \frac{\lambda}{g_2} N_{15}(N_{14} \sin\beta + N_{13} \cos\beta). \quad (3.2)$$

⁸This definition of R_{XY} is based on the fact that the Higgs production is SM-like for the setting in eqs. (2.11) and (2.12).

Here the quantities N_{1i} are the components of the lightest (unitary) eigenvector of the neutralino mass matrix $\mathcal{M}_{\tilde{\chi}^0}$ which is determined at one-loop after the RGEs flow achieved via **SPheno** and **SARAH** as explained in section 2.2. The quantity $m_{\tilde{\chi}_1^0}$ is the pole mass of the lightest eigenstate of $\mathcal{M}_{\tilde{\chi}^0}$. At tree level $\mathcal{M}_{\tilde{\chi}^0}$ reduces to

$$\mathcal{M}_{\tilde{\chi}^0}^{tree} = \begin{pmatrix} M_1 & 0 & -\frac{1}{2}g_1 v_1 & \frac{1}{2}g_1 v_2 & 0 \\ 0 & M_2 & \frac{1}{2}g_2 v_1 & -\frac{1}{2}g_2 v_2 & 0 \\ -\frac{1}{2}g_1 v_1 & \frac{1}{2}g_2 v_1 & 0 & -\mu & -\frac{1}{2}v_2 \lambda \\ \frac{1}{2}g_1 v_1 & -\frac{1}{2}g_2 v_2 & -\mu & 0 & -\frac{1}{2}v_1 \lambda \\ 0 & 0 & -\frac{1}{2}v_2 \lambda & -\frac{1}{2}v_1 \lambda & \mu_\Sigma \end{pmatrix}. \quad (3.3)$$

Notice that due to the LEP chargino mass constraint $m_{\tilde{\chi}_1^\pm} \gtrsim 100$ GeV, a lightest neutralino with mass $m_{\tilde{\chi}_1^0} < m_h/2$ must be predominantly Bino. The coupling $g_{h\tilde{\chi}_1^0\tilde{\chi}_1^0}$ is then dominated by the Higgsino and Bino mixings, namely $N_{11}N_{13}$ and $N_{11}N_{14}$. Consequently, for a given set of parameters, the experimental constraint on $\text{BR}(h \rightarrow \tilde{\chi}_1^0\tilde{\chi}_1^0)$ turns out to be a lower bound on μ .

When $m_{\tilde{\chi}_1^0}$ is even smaller, namely lighter than $m_Z/2$, also the LEP bound $\Gamma(Z \rightarrow \tilde{\chi}_1^0\tilde{\chi}_1^0) \lesssim 2$ MeV [45] has to be taken into account. As the constraint on $\text{BR}(h \rightarrow \tilde{\chi}_1^0\tilde{\chi}_1^0)$, it imposes a lower bound on μ once the other parameters are fixed. We quantify it by the expression

$$\Gamma(Z \rightarrow \tilde{\chi}_1^0\tilde{\chi}_1^0) = \frac{1}{12\pi} \frac{G_F}{\sqrt{2}} m_Z^3 \left(1 - \frac{4m_{\tilde{\chi}_1^0}^2}{m_Z^2}\right)^{3/2} (|N_{13}|^2 - |N_{14}|^2)^2. \quad (3.4)$$

Moreover, when Higgsinos are extremely heavy and the lightest (Bino-like) neutralino is below the threshold of about 20 GeV, the further channel $h \rightarrow \tilde{\chi}_2^0\tilde{\chi}_1^0$ may be kinematically open without any dangerous enhancement to the invisible width of the Higgs or Z bosons. However, being μ very large, the chargino $\tilde{\chi}_1^\pm$ and the neutralino $\tilde{\chi}_2^0$ are almost degenerate. The LHC analysis on three leptons plus missing energy [30] excludes the parameter region of this scenario where $\tilde{\chi}_2^0$ mostly decays into $Z^{(*)}\tilde{\chi}_1^0$. In the remaining region where the channel $\tilde{\chi}_2^0 \rightarrow h^{(*)}\tilde{\chi}_1^0$ competes, it is instead unclear what the experimental limits are. Determining them would require a specific analysis that goes beyond the scope of this study and we then conservatively focus on the region with $\text{BR}(h \rightarrow \tilde{\chi}^0\tilde{\chi}^0) = \text{BR}(h \rightarrow \tilde{\chi}_1^0\tilde{\chi}_1^0)$.

3.2 The $h \rightarrow \gamma\gamma$ channel

Since the Higgs production is SM-like, the diphoton signal strength $R_{\gamma\gamma}$ depends only on $\text{BR}(h \rightarrow \gamma\gamma)$. For our setting in eqs. (2.11) and (2.12) only charginos can induce deviations from the SM prediction of $\Gamma(h \rightarrow \gamma\gamma)$. Their contributions to $R_{\gamma\gamma}$ have been already calculated by means of the low-energy approximation [12, 18] or in the M_2 decoupling limit [27], starting from the tree-level chargino mass matrix

$$\mathcal{M}_{\tilde{\chi}^\pm}^{tree} = \begin{pmatrix} M_2 & g_2 v \sin \beta & 0 \\ g_2 v \cos \beta & \mu & -\lambda v \sin \beta \\ 0 & \lambda v \cos \beta & \mu_\Sigma \end{pmatrix}. \quad (3.5)$$

It has been observed that maximal diphoton enhancement occurs when all chargino mass parameters are light (compatibly with the chargino mass bound) and moreover, in the regime of very small $\tan\beta$ and large λ (linked one to each other by the Higgs mass constraint), when Triplino and Higgsino mass parameters are degenerate [18].

In the present analysis we improve the previous estimate by including loop-corrections in $\mathcal{M}_{\tilde{\chi}^\pm}$. In many cases these radiative contributions increase the lightest chargino mass by about 10% with respect to its tree-level value. They can hence be important when one cuts the allowed parameter space due to the LEP bound $m_{\tilde{\chi}_i^\pm} \gtrsim 100$ GeV.

When only charginos provide new (sizeable) contributions to the diphoton channel and the Higgs production is SM-like, $R_{\gamma\gamma}$ is given by

$$R_{\gamma\gamma} = \left| 1 + \frac{A_{\tilde{\chi}_{1,2,3}^\pm}^{\gamma\gamma}}{A_W^{\gamma\gamma} + A_t^{\gamma\gamma}} \right|^2, \quad (3.6)$$

$$A_{\tilde{\chi}_{1,2,3}^\pm}^{\gamma\gamma} = \sum_{i=1}^3 \frac{2M_W}{\sqrt{2} m_{\tilde{\chi}_i^\pm}} (g_{h\tilde{\chi}_i^+ \tilde{\chi}_i^-}^L + g_{h\tilde{\chi}_i^+ \tilde{\chi}_i^-}^R) A_{1/2}(\tau_{\tilde{\chi}_i^\pm}), \quad (3.7)$$

where $A_{1/2}$ is the spin-1/2 scalar function (see e.g. ref. [46] for its explicit expression) with argument $\tau_{\tilde{\chi}_i^\pm} = m_h^2/4m_{\tilde{\chi}_i^\pm}^2$, and $g_{h\tilde{\chi}_i^+ \tilde{\chi}_i^-}$ is the lightest Higgs effective coupling to charginos. The quantities $A_W^{\gamma\gamma}$ and $A_t^{\gamma\gamma}$ are the W -boson and top-quark contributions whose values are respectively -8.3 and 1.9 for $m_h \simeq 126$ GeV.

In the procedure we apply, which corresponds to the one **SPheno** and **SARAH** employ, $R_{\gamma\gamma}$ is calculated by plugging the chargino pole masses into $A_{1/2}(\tau_{\tilde{\chi}_i^\pm})$. Moreover, the couplings $g_{h\tilde{\chi}_i^+ \tilde{\chi}_i^-}^R$ and $g_{h\tilde{\chi}_i^+ \tilde{\chi}_i^-}^L$ are the particular case $i = j$ of the expressions

$$g_{h\tilde{\chi}_i^+ \tilde{\chi}_j^-}^L = \frac{1}{\sqrt{2}} \left[\left(U_{j1} V_{i2} - \frac{\lambda}{g_2} U_{j2} V_{i3} \right) \sin\beta + \left(U_{j2} V_{i1} + \frac{\lambda}{g_2} U_{j3} V_{i2} \right) \cos\beta \right], \quad (3.8)$$

$$g_{h\tilde{\chi}_i^+ \tilde{\chi}_j^-}^R = \frac{1}{\sqrt{2}} \left[\left(U_{i1} V_{j2} - \frac{\lambda}{g_2} U_{i2} V_{j3} \right) \sin\beta + \left(U_{i2} V_{j1} + \frac{\lambda}{g_2} U_{i3} V_{j2} \right) \cos\beta \right], \quad (3.9)$$

where U and V are the unitary matrices diagonalizing the one-loop chargino mass matrix $\mathcal{M}_{\tilde{\chi}^\pm}$ such that $U\mathcal{M}_{\tilde{\chi}^\pm}V^T = \text{diag}(m_{\tilde{\chi}_1^\pm}, m_{\tilde{\chi}_2^\pm}, m_{\tilde{\chi}_3^\pm})$.

3.3 The $h \rightarrow Z\gamma$ channel

LHC constraints on $R_{Z\gamma}$ are still very weak [47, 48]. Nevertheless, the $h \rightarrow Z\gamma$ channel, likewise the $h \rightarrow \gamma\gamma$ decay, is worth to analyze since it is particularly sensitive to new colorless electrically-charged particles which do not change the Higgs production. At the best of our knowledge, in the TMSSM the $R_{Z\gamma}$ signal strength has never been calculated.

Similarly to the case of $R_{\gamma\gamma}$, for our setting (2.11) and (2.12) only charginos can move $\Gamma(h \rightarrow Z\gamma)$ from its SM value. This leads to

$$R_{Z\gamma} = \left| 1 + \frac{A_{\tilde{\chi}_{1,2,3}^\pm}^{Z\gamma}}{A_W^{Z\gamma} + A_t^{Z\gamma}} \right|^2. \quad (3.10)$$

The contributions $A_W^{Z\gamma}$ and $A_t^{Z\gamma}$ have been first obtained in refs. [49, 50]. They can be expressed in term of Passarino-Veltman three-point functions and turn out to be $A_W^{Z\gamma} = -12$ and $A_t^{Z\gamma} = 0.6$ for $m_h \simeq 126$ GeV [51].

In the TMSSM the chargino contribution comes from triangular loops where all three chargino mass-eigenstates run in and can be flipped from one to another at the vertices (both clockwise and anti-clockwise helicity directions must be taken into account). No flipping however occurs at the vertex involving the photon. For this reason only up to two chargino mass-eigenstates run inside a given loop and each diagram involves a loop integration that is formally similar to those arising in the MSSM calculation (where only two charginos exist). Consequently the study of the $\Gamma(h \rightarrow Z\gamma)$ is a straightforward generalization to three charginos of the MSSM expression given in ref. [51].

In the view of the above considerations, we can generalize the procedure of ref. [51] and we obtain

$$A_{\tilde{\chi}_{1,2,3}^\pm}^{Z\gamma} = \sum_{j,k=1}^3 \frac{g_2 m_{\tilde{\chi}_j^\pm}}{g_1 m_Z} f(m_{\tilde{\chi}_j^\pm}, m_{\tilde{\chi}_k^\pm}, m_{\tilde{\chi}_k^\pm}) (g_{h\tilde{\chi}_j^+\tilde{\chi}_i^-}^L + g_{h\tilde{\chi}_j^+\tilde{\chi}_i^-}^R)(g_{Z\tilde{\chi}_j^+\tilde{\chi}_i^-}^L + g_{Z\tilde{\chi}_j^+\tilde{\chi}_i^-}^R), \quad (3.11)$$

in which: f is a linear combination of Passarino-Veltman functions defined in ref. [51]; $m_{\tilde{\chi}_j^\pm}$ are pole masses; $g_{h\tilde{\chi}_j^+\tilde{\chi}_i^-}^L$ and $g_{h\tilde{\chi}_j^+\tilde{\chi}_i^-}^R$ are provided in eqs. (3.8) and (3.9); $g_{Z\tilde{\chi}_j^+\tilde{\chi}_i^-}^L$ and $g_{Z\tilde{\chi}_j^+\tilde{\chi}_i^-}^R$ are given by

$$g_{Z\tilde{\chi}_i^+\tilde{\chi}_j^-}^R = - \left(V_{i1}V_{j1}^* + \frac{1}{2}V_{i2}V_{j2}^* + V_{i3}V_{j3}^* - \delta_{ij}s_W^2 \right), \quad (3.12)$$

$$g_{Z\tilde{\chi}_i^+\tilde{\chi}_j^-}^L = - \left(U_{i1}U_{j1}^* + \frac{1}{2}U_{i2}U_{j2}^* + U_{i3}U_{j3}^* - \delta_{ij}s_W^2 \right). \quad (3.13)$$

4 Numerical analysis setup

The TMSSM involves several free parameters. Some of them have to be fixed for practical purposes but play no role in our analysis. This is the case for the whole slepton sector whose masses are assumed above the TeV scale not to interfere with the chargino and neutralino phenomenology we analyze. Other parameters have a minor impact, and their choice given in eq. (2.11) is motivated in section 2.1. Some have to satisfy the EWSB conditions (as explained in section 2.2), and finally only the followings are still undetermined:

$$\{\theta_i\} = \{M_1, M_2, \mu, \mu_\Sigma, \tilde{m}, \tan \beta, \lambda\}. \quad (4.1)$$

To accomplish an efficient sampling on these seven parameters, we adopt an approach based on Bayes' theorem

$$p(\theta_i|d) \propto \mathcal{L}(d|\theta_i)\pi(\theta_i), \quad (4.2)$$

where d are the data under consideration, $\mathcal{L}(d|\theta_i)$ is the likelihood function and $p(\theta_i|d)$ is the posterior Probability Distribution Function (PDF). The function $\pi(\theta_i)$ is the prior PDF, it is independent of data and describes our belief on the values of the theoretical parameter, before the confrontation with experimental results.

Table 1. Nested Sampling (NS) parameters and their prior ranges. The priors are flat over the indicated range.

NS parameters	Prior range
$\log_{10}(M_1/\text{GeV}), \log_{10}(\mu_{\Sigma}/\text{GeV})$	$1 \rightarrow 3$
$\log_{10}(\mu/\text{GeV}), \log_{10}(M_2/\text{GeV})$	$2 \rightarrow 3$
\tilde{m}/TeV	$0.63 \rightarrow 2$
$\log_{10}(\tan \beta)$	$0 \rightarrow 1$
λ	$0.5 \rightarrow 1.2$

All priors $\pi(\theta_i)$ used in the analysis and their ranges of variation are summarized in table 1. A flat prior is assumed for the stop parameter \tilde{m} , with an upper bound at 2 TeV in order not to introduce a large electroweak fine-tuning. For gaugino, Higgsino and Triplino masses, we instead consider logarithm priors and values below the TeV scale. Such a choice is aimed to improve the statistics in the parameter space where charginos tend to be close to their LEP mass bound, may enhance $R_{\gamma\gamma}$ and $R_{Z\gamma}$, and may open the window of the lightest neutralino DM particle. For the same purpose, and in order not to barely reproduce a MSSM-like phenomenology, we also impose $\tan \beta$ smaller than 10. A similar reasoning applies for the chosen range for λ . Within such values we expect to fully cover the TMSSM parameter region where the little hierarchy problem is alleviated (with respect to the MSSM) and perturbation theory does not break down before the GUT scale [12]. On the other hand, we neither exclude a priori scenarios with Landau poles at the PeV scale because these may be avoided in ultraviolet completions of the TMSSM.

The likelihood function is the conditional probability of the data given the theoretical parameters. The data d used in $\mathcal{L}(d|\theta_i)$, which are the observables and constraints summarized in table 2, are as follows.

Collider data: We require the lightest CP-even Higgs mass m_h to be compatible with the ATLAS and CMS measurements [1, 2], which we (indicatively) combine by a statistical mean. Its uncertainty is dominated by the theoretical error, which is estimated to be around 3 GeV [42]. We also assume chargino and stop masses that fulfill the bounds $m_{\tilde{\chi}_1^\pm} > 101$ GeV [28] and $m_{\tilde{t}_1} > 650$ GeV [30]. Finally, we require the invisible decay width of the Z boson to be smaller than 2 MeV [45].

DM data: We impose the lightest neutralino relic abundance to match $\Omega_{\text{DM}}h^2$ measured by Planck [52], as we are interested only in single-component DM. Notice that the experimental error on this observable has become incredibly smaller than the theoretical one, hence we consider an additional 20% of theoretical uncertainty [53]. Furthermore, we enforce the neutralino SI cross-section off nuclei, σ_n^{SI} , to be compatible with the LUX direct detection exclusion bound [26] at 90% CL. For the theoretical prediction of the SI cross-section mediated by the Higgs boson, we do not introduce uncertainties related to the strange quark content of the nucleon: we fix the ratio of nucleon mass and strange quark mass to be $f_s = 0.053$ MeV, accordingly to ref. [54] (for effects due to different choices of

Table 2. Summary of the observables and constraints used in this analysis.

Type	Observable	Measurement/Limit	Ref.
<i>Collider data</i>	m_h	125.85 ± 0.4 GeV (exp) ± 3 GeV (theo)	[1, 2]
	$\Gamma(Z \rightarrow \tilde{\chi}_1^0 \tilde{\chi}_1^0)$	< 2 MeV	[28]
	$m_{\tilde{t}_1}$	> 650 GeV (LHC 90% CL)	[30]
	$m_{\tilde{\chi}_1^+}$	> 101 GeV (LEP 95% CL)	[28]
<i>DM data</i>	$\Omega_{\text{DM}} h^2$	0.1186 ± 0.0031 (exp) $\pm 20\%$ (theo)	[52]
	σ_{Xe}^{SI}	LUX (90% CL)	[26]

f_s and similar quantities such as $\sigma_{\pi n}$ see e.g. refs. [55–59]).

For either the relic density and the Higgs mass we use a Gaussian likelihood function whose peak corresponds to the measured central value and whose width reproduces the standard deviation of the measurement (explicit quantities are quoted in table 2). For the σ_n^{SI} constraint we instead implement a Heaviside likelihood function. The DM constraints are implemented in the likelihood function $\mathcal{L}_{\text{DM}}(d|\theta_i)$, the collider constraints are implemented in the likelihood function $\mathcal{L}_{\text{Coll}}(d|\theta_i)$ and the full likelihood is simply the product of every individual likelihood associated to an experimental result. Finally, the above stop and chargino mass limits as well as the constraint on the Z -boson invisible width are absorbed into the prior PDFs: each parameter point generating a TMSSM mass spectrum that violates these bounds is discarded.

For some given values of the theoretical inputs θ_i the collider and DM observables are computed by means of some public codes. We briefly summarize the programming procedure. We employ `SARAH-3.3.0` and `SPheno-3.2.4` to calculate the TMSSM mass spectrum (where radiative corrections are taken into account as described in section 2.2). Also $\Gamma(Z \rightarrow \tilde{\chi}_1^0 \tilde{\chi}_1^0)$, $\text{BR}(h \rightarrow \tilde{\chi}_1^0 \tilde{\chi}_1^0)$, $R_{\gamma\gamma}$ and $R_{Z\gamma}$ are determined by dint of `SPheno-3.2.4` along the lines of section 3 (for $R_{Z\gamma}$ we also use the Passarino-Veltman functions that are implemented in the `CPsuperH2.3` libraries [60]). Afterward, the `SPheno-3.2.4` output is elaborated by `micrOMEGAs_2.4.5` [61]. In this way we compute the DM observables listed in table 2.

To explore the parameter space we link `SPheno` and `micrOMEGAs_2.4.5` to the nested sampling algorithm `MultiNest_v3.2` [62] (with specifications of 4000 live points and tolerance parameter set to 0.5). This algorithm produces the posterior samples from distributions with a large number of parameters and with multi-modal likelihoods more efficiently than Markov Chain Monte Carlo. At practical level we run two samples: for analyzing the Higgs phenomenology we use only $\mathcal{L}_{\text{Coll}}(d|\theta_i)$ (sample 1), whereas when exploring the DM constraints as well, we use the full likelihood (sample 2). `MultiNest_v3.2` might however populate with an insufficient number of points regions where the likelihood is flat. This is relevant for the $R_{\gamma\gamma}$ and $R_{Z\gamma}$ observables, as we do not impose constraints on their values in the likelihood function. To address this issue we run two additional samples with $\mathcal{L}(d|\theta_i)_3 = \mathcal{L}_{\text{Coll}}(d|\theta_i) \times \mathcal{L}_{\gamma\gamma}(d|\theta_i)$ and $\mathcal{L}(d|\theta_i)_4 = \mathcal{L}_{\text{Coll}}(d|\theta_i) \times \mathcal{L}_{\text{DM}}(d|\theta_i) \times \mathcal{L}_{\gamma\gamma}(d|\theta_i)$ (for the

case without and with the DM constraints respectively, sample 3 and sample 4). These two likelihood functions include a *fake* information associated to an extra Gaussian likelihood function $\mathcal{L}_{\gamma\gamma}(d|\theta_i)$ with $R_{\gamma\gamma} = 1.6 \pm 0.2$ to ensure a efficient exploration of region with large $h \rightarrow \gamma\gamma$ and $h \rightarrow \gamma Z$ signal strengths⁹. We do not provide a statistical analysis of the samples but show the result for points drawn randomly from the posterior PDF, which are provided in the `*post_equal_weight.dat` file constructed by `MultiNest.v3.2`, hence we can safely combine the samples originating from different run with different likelihood functions. Before discussing our findings, let us mention some experimental bounds that we do not enforce in the sampling phase.

Different bounds on $\text{BR}(h \rightarrow \tilde{\chi}_1^0 \tilde{\chi}_1^0)$ exist in the literature [43, 44, 63–66]. Imposing any of them would make our results of difficult interpretation if a different bound should be considered. We thus prefer not imposing any cut on $\text{BR}(h \rightarrow \tilde{\chi}_1^0 \tilde{\chi}_1^0)$ and just presenting its value in the results we present.

We are also aware of the bounds on the chargino and neutralino masses based on simplified models: in scenarios with $m_{\tilde{\chi}_1^0} \lesssim 100 \text{ GeV}$ and $m_{\tilde{\chi}_1^\pm} \simeq m_{\tilde{\chi}_2^0}$, data analyses impose $m_{\tilde{\chi}_1^\pm} \gtrsim 350 \text{ GeV}$ at 95% CL if $\tilde{\chi}_2^0$ decays 100% into Z boson, or $m_{\tilde{\chi}_1^\pm} \gtrsim 170 \text{ GeV}$ if $\tilde{\chi}_2^0$ decays 100% into h boson [67, 68]. However, due to its not straightforward interpretation in the generic TMSSM parameter space, we do not impose such constraints. Instead, in the post processing phase of the samples we verify that these bounds do not apply in the interesting ballpark of our analysis. Indeed, in particular when we achieve a relevant diphoton enhancement, the fields $\tilde{\chi}_2^0$ and $\tilde{\chi}_2^\pm$ are mixed states and consequently (i) their masses are not degenerate and (ii) the neutralino decay channels into Z and h bosons can compete especially due the Triplino component and its potentially sizeable coupling λ .

Finally, we also consider the $B_s \rightarrow \mu^+ \mu^-$ and $B \rightarrow X_s \gamma$ observables and the neutralino Spin-Dependent (SD) cross-section off protons and neutrons. We use `SPheno-3.2.4` and `micrOMEGAs.2.4.5` respectively to calculate them. As expected in scenarios with low $\tan \beta$, these B -meson signatures are in full agreement with experiments [69, 70]. We will compare the results for SD cross-section with COUPP and XENON100 limits [71, 72] on proton and neutron respectively and comment them in section 6.

5 $R_{Z\gamma}$ and $R_{\gamma\gamma}$ without DM constraints

Within the TMSSM, the possibility of achieving sizeable enhancements in $R_{\gamma\gamma}$ has been previously highlighted in refs. [12, 18]. These analyses were performed by considering tree-level chargino masses and low-energy limit approximations. They were moreover carried out for some illustrative parameter regions. In this section we extend the previous analysis focused on the $m_A \gg m_h$ regime [12]. In particular, we explore a broader parameter space (but still keeping large m_A) and we include the radiative effects discussed in section 3.2. We also present our findings for $R_{Z\gamma}$ in eq. (3.10).

Before reporting the result of the full parameter sampling, it is educative to understand the role of some inputs. The essential parameter dependence of $R_{\gamma\gamma}$ and $R_{Z\gamma}$ is shown in

⁹We check that the upper bounds on $R_{\gamma\gamma}$ and $R_{Z\gamma}$ we will obtain do not change by requiring large $R_{Z\gamma}$ instead of high $R_{\gamma\gamma}$.

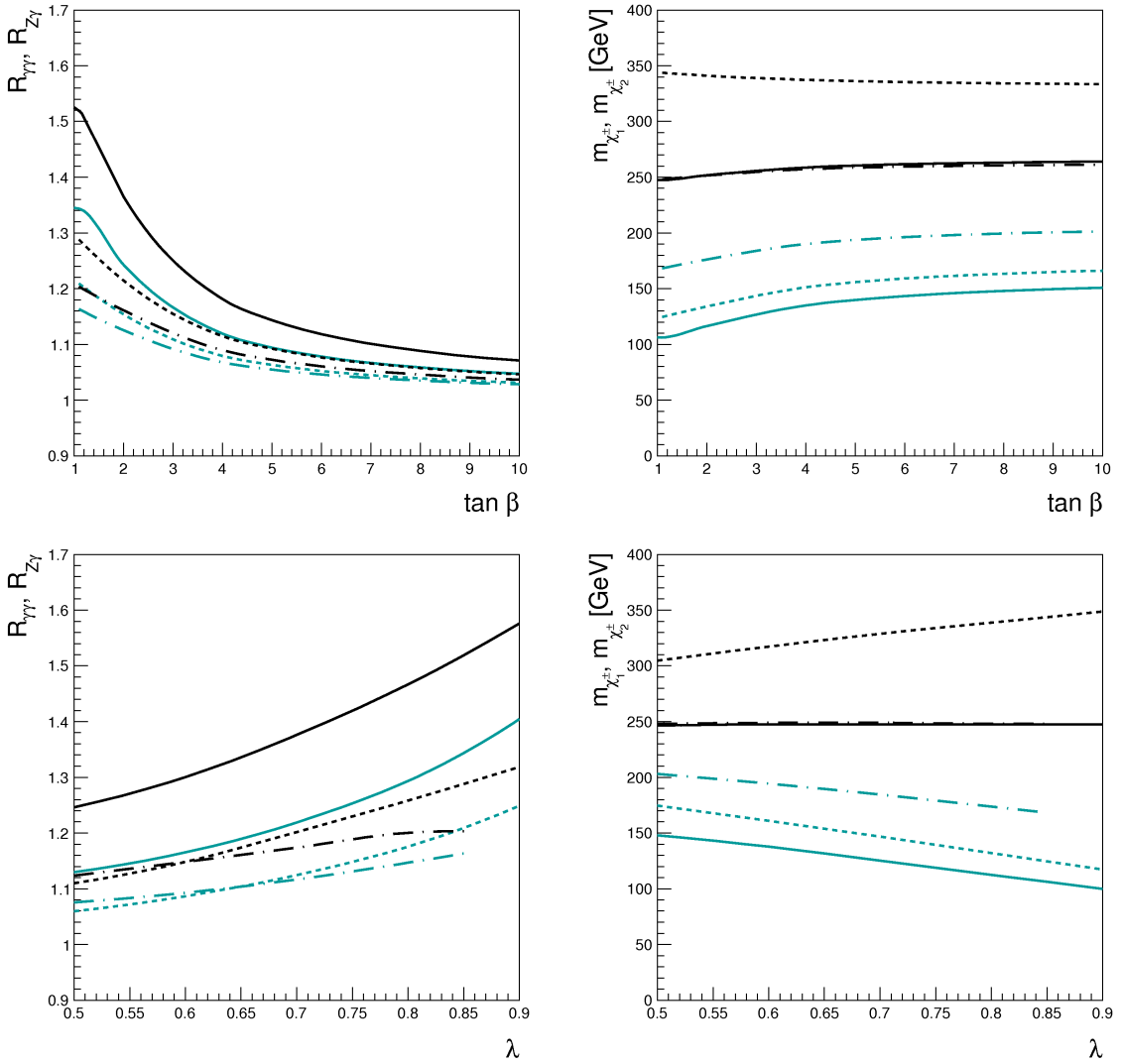


Figure 2. *Top left:* Analytic behavior of $R_{\gamma\gamma}$ (black) and $R_{Z\gamma}$ (turquoise) as a function of $\tan\beta$ for $\lambda = 0.85$. The solid lines are for $\mu = \mu_\Sigma = M_2 = 230$ GeV (scenario A), the dashed lines stand for $\mu = \mu_\Sigma = 230$ GeV, $M_2 = 1$ TeV (scenario B) and the dot-dash lines for $\mu_\Sigma = M_2 = 230$ GeV, $\mu = 400$ GeV (scenario C). *Top right:* Dependence on $\tan\beta$ of the lightest (turquoise) and next to lightest (black) chargino masses, which contribute to the $R_{\gamma\gamma}$ and $R_{Z\gamma}$ shown in the left panel (the solid/dashing code is as in the left panel). *Bottom:* Same as above as a function of λ for $\tan\beta = 1.1$.

the left panels of figure 2. In the figure we assume the setting in eq. (2.11), as well as $\lambda = 0.85$ in the upper plot and $\tan\beta = 1.1$ in the lower one. At each point the stop parameter \tilde{m} is adjusted to obtain $m_h = 126$ GeV. The signal strengths $R_{\gamma\gamma}$ and $R_{Z\gamma}$ (black and turquoise lines, respectively) are calculated for three chargino mass settings: $\mu = \mu_\Sigma = M_2 = 230$ GeV (solid curves; scenario A), $\mu = \mu_\Sigma = 230$ GeV, $M_2 = 1$ TeV (dashed curves; scenario B) and $\mu_\Sigma = M_2 = 230$ GeV, $\mu = 400$ GeV (dotted-dashed curves;

scenario C). The corresponding chargino masses $m_{\tilde{\chi}_1^\pm}$ and $m_{\tilde{\chi}_2^\pm}$ are presented in the right panels by employing the same mark code of the left plots.

For the parameter choice considered in the figure, the enhancement in $h \rightarrow \gamma\gamma$ is always larger than the one in $h \rightarrow Z\gamma$. Moreover, $R_{\gamma\gamma}$ and $R_{Z\gamma}$ are strongly correlated and a sizeable enhancement in $R_{\gamma\gamma}$ requires a departure from the SM also in the $h \rightarrow Z\gamma$ channel. These behaviors will be confirmed in the results of the full parameter sampling.

As figure 3 shows, in each scenario the largest $R_{\gamma\gamma}$ and $R_{Z\gamma}$ are achieved by reducing $\tan\beta$ and increasing λ , which also corresponds to requiring less tuning in the electroweak sector (cf. eq. (2.10)). The enhancement is mostly due to the decrease of $m_{\tilde{\chi}_1^\pm}$ and the consequent smaller suppression of the loop functions in eqs. (3.6) and (3.11) (cf. right panels of the figure; the masses $m_{\tilde{\chi}_{2,3}^\pm}$ are large in the three scenarios and hence provide a subleading effect). However, also the coupling $g_{h\tilde{\chi}_1^\pm\tilde{\chi}_1^\pm}$ plays an important role. This can be deduced by comparing $R_{\gamma\gamma}$ (or $R_{Z\gamma}$) in different scenarios in correspondence to the same $m_{\tilde{\chi}_1^\pm}$ value. For instance, for $\lambda = 0.85$ both scenario A with $\tan\beta \simeq 10$ and scenario B with $\tan\beta \simeq 1.1$ have the same chargino mass $m_{\tilde{\chi}_1^\pm} \simeq 150$ GeV but quite different $R_{\gamma\gamma}$. These observations are in agreement with previous results obtained for $R_{\gamma\gamma}$ [12, 15, 16].

A last remark concerns the parameter range of figure 2. We do not enter the regime of $\tan\beta \simeq 1$ and $\lambda \gtrsim 1$ to achieve larger enhancements. Besides the reasons previously provided, there is a further issue that imposes such a restriction: the more the tree-level Higgs mass is boosted, the smaller the radiative corrections have to be not to overstep the $m_h \simeq 126$ GeV constraint. In particular, this may require stop masses below the bound of table 2, as it happens in scenario C at $\lambda \gtrsim 0.85$ with $\tan\beta \lesssim 1.1$. Of course, slightly bigger enhancements would exist by allowing for $m_{\tilde{t}} \ll 650$ GeV and/or $m_\Sigma \ll 5$ TeV. However, since proving the experimental suitability of such modifications would require specific collider analyses, and lowering m_Σ may also increase the electroweak fine tuning, we do not further discuss this possibility.

The two samples obtained with $\mathcal{L}_{\text{Coll}}(d|\theta_i)$ are presented in figure 3. The amount of diphoton enhancement is encoded in the color of the points: $R_{\gamma\gamma} < 1.1$ in gray, $1.1 < R_{\gamma\gamma} < 1.2$ in blue, $1.2 < R_{\gamma\gamma} < 1.3$ in green, $1.3 < R_{\gamma\gamma} < 1.4$ in brown, and $R_{\gamma\gamma} > 1.4$ in yellow (this color code will be maintained in the rest of the paper). The bottom left panel of the figure proves that the presence of the Triplino is fundamental to achieve $R_{\gamma\gamma} \gtrsim 1.3$. Indeed, if the Triplino component of the lightest chargino is negligible, $R_{\gamma\gamma}$ falls to MSSM-like values, i.e. $R_{\gamma\gamma} \lesssim 1.2$ [16]¹⁰. However, in some extreme cases, Triplino effects may be still present even when μ_Σ is quite large and the Triplino component of the lightest chargino is subdominant (but not negligible), as the case $\mu_\Sigma \simeq 900$ GeV and $R_{\gamma\gamma} \gtrsim 1.4$ shows.

The features of the parameter regions where the yellow points accumulate can be explained as follows. As observed in figure 2, large diphoton enhancements are allowed for small $\tan\beta$ and rather large λ (cf. bottom right panel). In such a case, the relation

¹⁰This MSSM upper bound on $R_{\gamma\gamma}$ is obtained by assuming a mass spectrum similar to ours, where only charginos can enhance the diphoton rate. Due to different crucial assumptions, we do not compare our results to those of refs. [5, 15].

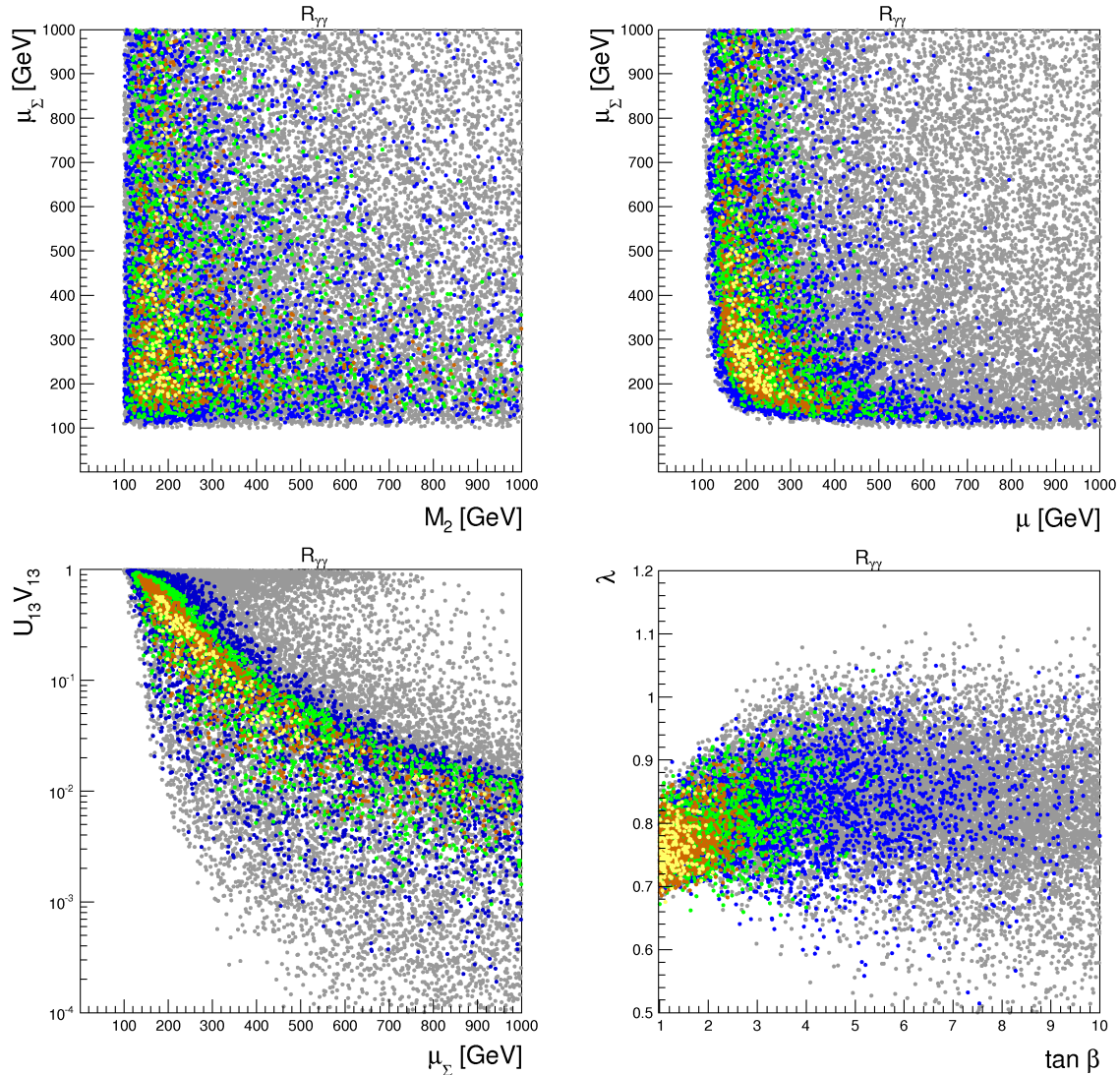


Figure 3. *Top left:* $R_{\gamma\gamma}$ (third direction) projected in the $\{\mu_\Sigma - M_2\}$ -plane. The values of $R_{\gamma\gamma}$ are encoded in the colors: $R_{\gamma\gamma} < 1.1$ in gray, $1.1 \leq R_{\gamma\gamma} < 1.2$ in blue, $1.2 \leq R_{\gamma\gamma} < 1.3$ in green, $1.3 \leq R_{\gamma\gamma} < 1.4$ in brown, and $R_{\gamma\gamma} \geq 1.4$ in yellow. *Top right:* Same as left in the $\{\mu_\Sigma - \mu\}$ -plane. *Bottom left and right:* Same as top left for the Triplino component of the lightest chargino as a function of μ_Σ and $\{\lambda - \tan \beta\}$ -plane respectively.

$\lambda > g_2$ arises. Consequently, in the Higgs-chargino-chargino coupling the contribution proportional to λ can push $g_{h\tilde{\chi}_1^\pm\tilde{\chi}_1^\pm}^{L,R}$ above the maximal value obtained in the MSSM. This of course occurs only if both Triplino and Higgsino components are unsuppressed. Large $R_{\gamma\gamma}$ enhancements then require μ and μ_Σ at the electroweak scale (cf. top right panel). On the other hand, also the MSSM-like contribution of the Higgs-chargino-chargino coupling can provide an additional boost to $g_{h\tilde{\chi}_1^\pm\tilde{\chi}_1^\pm}^{L,R}$ if the Wino mixing is sizeable. Therefore, also M_2 has to be small to achieve maximal enhancements (cf. top left plot). In particular, in order to minimally suppress the loop function $A_{1/2}(\tau_{\tilde{\chi}_i^\pm})$, the parameters have to be

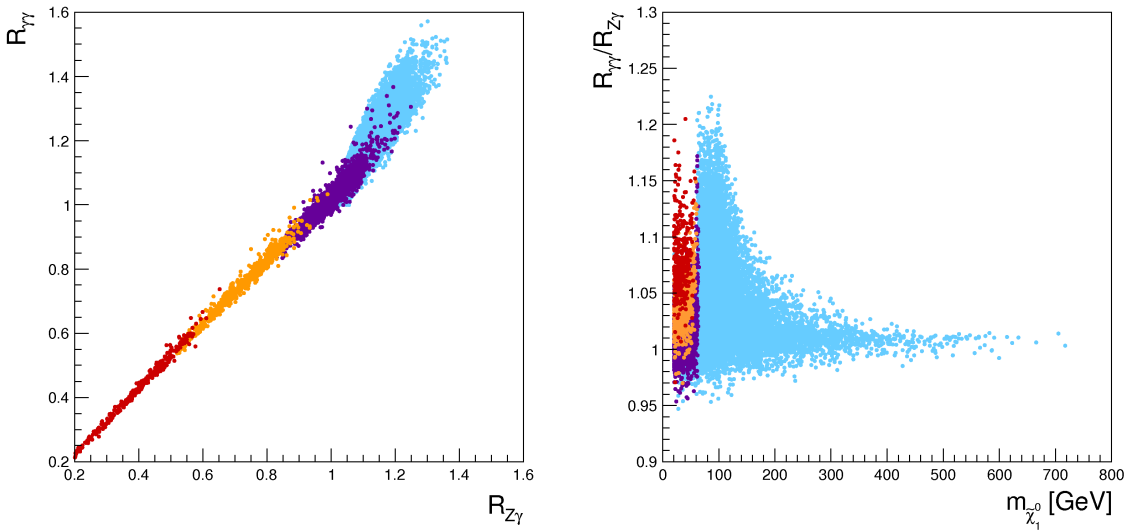


Figure 4. Correlation between $R_{\gamma\gamma}$ and $R_{Z\gamma}$ for the equal weight posterior sample. The color code is: light blue for $\text{BR}(h \rightarrow \tilde{\chi}_1^0 \tilde{\chi}_1^0) < 1\%$, violet for $1\% < \text{BR}(h \rightarrow \tilde{\chi}_1^0 \tilde{\chi}_1^0) < 20\%$, dark yellow for $20\% < \text{BR}(h \rightarrow \tilde{\chi}_1^0 \tilde{\chi}_1^0) < 50\%$ and red for $\text{BR}(h \rightarrow \tilde{\chi}_1^0 \tilde{\chi}_1^0) > 50\%$.

correlated in such a way that $m_{\tilde{\chi}_1^\pm} \approx 101$ GeV.

The effect of the Higgs and stop mass constraints is pointed out in the bottom right panel of the figure. The region with small λ and small $\tan\beta$ is not populated because the tree-level Higgs mass (2.10) is very small. In such a case, only large stop loop corrections to m_h could push it up to 126 GeV, but such corrections are not allowed due to the \tilde{m} range of table 1. On the contrary, in the upper empty area with small $\tan\beta$, the tree-level Higgs mass is too large. In this case stop loop corrections have to be small not to overstep the Higgs mass constraint, but they are incompatible with the bound $m_{\tilde{\tau}_1} > 650$ GeV. Curiously, the mass bound cuts off most of the parameter space where the TMSSM exhibits a Landau pole at a scale $Q \lesssim 10^8$ GeV (see ref. [12] for estimates of the Landau pole scale). We stress however that the border of this empty region could be mildly moved by considering larger values of M_2, μ , and μ_Σ than those in table 1. Heavier charginos would indeed provide bigger (negative) radiative correction to m_h that should be compensated by slightly larger stop masses to keep $m_h \approx 126$ GeV [37].

Although figure 3 presents only $R_{\gamma\gamma}$ results, the above considerations apply also to $R_{Z\gamma}$. Indeed, in the TMSSM $R_{\gamma\gamma}$ and $R_{Z\gamma}$ are tightly correlated. This is proven in figure 4, which displays the values of $R_{\gamma\gamma}$ and $R_{Z\gamma}$ arising in the samples 1 and 2. Since the sampling also explores the region with small M_1 , the $h \rightarrow \tilde{\chi}_1^0 \tilde{\chi}_1^0$ channel can be open. Depending on the value of $\text{BR}(h \rightarrow \tilde{\chi}_1^0 \tilde{\chi}_1^0)$, the points in the figure are colored as follows: $\text{BR}(h \rightarrow \tilde{\chi}_1^0 \tilde{\chi}_1^0) < 1\%$ in light blue, $1\% \leq \text{BR}(h \rightarrow \tilde{\chi}_1^0 \tilde{\chi}_1^0) < 20\%$ in violet, $20\% \leq \text{BR}(h \rightarrow \tilde{\chi}_1^0 \tilde{\chi}_1^0) < 50\%$ in dark yellow and $\text{BR}(h \rightarrow \tilde{\chi}_1^0 \tilde{\chi}_1^0) \geq 50\%$ in red (this color code will be followed in the rest of the paper).

In the left panel of the figure, the light blue area is not aligned with the remaining region. We have investigated the origin of this feature and it seems related to the different

kinds of configurations of chargino parameters in that region. In fact, in the upper-left part of the light blue area, the typical chargino configuration yields to very large $g_{h\tilde{\chi}_1^0\tilde{\chi}_1^0}^{L,R}$ (for $M_1 \lesssim 100$ GeV). Therefore, only when $m_{\tilde{\chi}_1^0}$ is tuned just below the $m_h/2$ threshold, $\text{BR}(h \rightarrow \tilde{\chi}_1^0\tilde{\chi}_1^0)$ is small. Unless of this rare accident, $\text{BR}(h \rightarrow \tilde{\chi}_1^0\tilde{\chi}_1^0)$ is either huge or zero. Consequently, for the configurations of chargino parameters that populate the upper-left part of the light blue area, $R_{\gamma\gamma}$ and $R_{Z\gamma}$ are typically either larger or much smaller than one, and an empty region at $R_{\gamma\gamma} \approx 1$ and $R_{Z\gamma} \approx 0.9$ is thus produced.

The opposite effect instead occurs in the lower part of the light blue region: the typical chargino parameters yield tiny $g_{h\tilde{\chi}_1^0\tilde{\chi}_1^0}^{L,R}$ and hence $\text{BR}(h \rightarrow \tilde{\chi}_1^0\tilde{\chi}_1^0)$ is small for very most of the values that M_1 can assume. For these configurations of chargino parameters, therefore, $R_{\gamma\gamma}$ and $R_{Z\gamma}$ do not jump from one value to a very different one at the threshold $m_{\tilde{\chi}_1^0} \sim m_h/2$ but slowly change as function of M_1 . For this reason the violet region is abundantly populated by such chargino configurations.

Finally, let us summarize the most striking result of this section. From our analysis we obtain the following TMSSM bounds (see figure 3):

$$R_{\gamma\gamma} \lesssim 1.6, \quad R_{Z\gamma} \lesssim 1.4, \quad 0.95 \lesssim R_{\gamma\gamma}/R_{Z\gamma} \lesssim 1.2 \quad (\text{no DM obs.}) \quad (5.1)$$

and we stress the tight degree of correlation between the two loop-induced processes. We will comment on the future experimental implications of these bounds in the conclusions (section 7).

6 DM phenomenology and constraints on $R_{\gamma\gamma}$ and $R_{Z\gamma}$

In this section we present the TMSSM phenomenology in the presence of a neutralino DM candidate. As previously motivated, we require that no supersymmetric particle but neutralinos and charginos interferes during freeze-out, to achieve the correct relic density. To understand the relevant consequences of introducing the Triplino component, we first analyze the Wino decoupling limit.

In figure 5 (left panel) the behaviors of the lightest-neutralino relic density and SI cross-section (black and red lines, respectively) for the limit $M_2 \gg 1$ TeV are depicted as a function of M_1 . The corresponding masses $m_{\tilde{\chi}_1^0}, m_{\tilde{\chi}_2^0}, m_{\tilde{\chi}_1^\pm}$ (left panel) and the lightest neutralino compositions (right panel) are also displayed by the mark code reported in the legends. The choice $\mu = 500$ GeV, $\mu_\Sigma = 180$ GeV, $\tan\beta = 2.9$ and $\lambda = 0.88$ is assumed. The SI cross-section is normalized to 10^{-9} pb, which is close to the maximum of LUX sensitivity given by $\sigma^{\text{SI}} \lesssim 8 \times 10^{-10}$ pb at $m_{\tilde{\chi}_1^0} \sim 50$ GeV [26].

It results that at low M_1 the lightest neutralino, which is almost pure Bino, overcloses the Universe until it reaches the Higgs resonance. In this region the lightest neutralino can provide the correct relic density and, moreover, its SI cross-section is below the LUX upper bound (i.e. the red curve is below 0.8). This occurs because the Higgsino components in the coupling $g_{h\tilde{\chi}_1^0\tilde{\chi}_1^0}$ is enough suppressed to be compatible with LUX results. The Higgs pole region is only mildly sensitive to the presence of the Triplino. For different parameter configurations, the correct relic density is achieved also at the Z boson resonance. We will discuss these two poles more in detail in section 6.2.

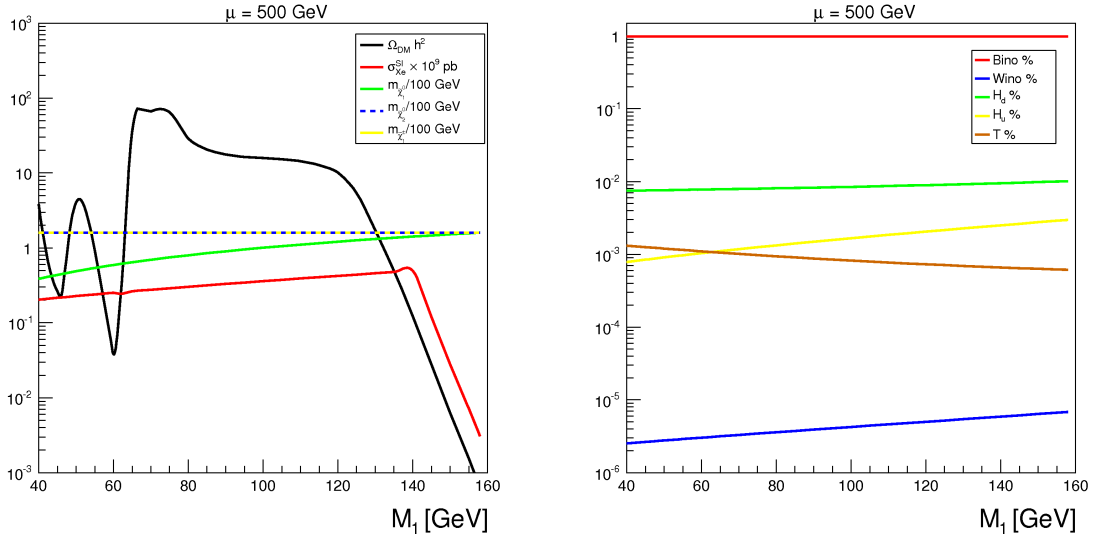


Figure 5. *Left:* Dependence of several physical quantities on M_1 : the black line denotes $\Omega_{\text{DM}} h^2$, the red $\sigma_{Xe}^{SI} \times 10^9 \text{ pb}$, the green the LSP, the blue $m_{\tilde{\chi}_2^0}$, the yellow $m_{\tilde{\chi}_1^\pm}$. The lightest chargino is degenerate with the next-to-lightest neutralino. *Right:* Component of LSP as a function of M_1 : in red is the Bino fraction, in brown the Triplino, in yellow and green the two Higgsino components and in blue the Wino fraction (as labelled in the caption). In both panels $\mu = 500 \text{ GeV}$, $M_2 = 1.5 \text{ TeV}$, $\mu_\Sigma = 180 \text{ GeV}$, $\tan \beta = 2.9$ and $\lambda = 0.88$.

Above the Higgs resonance, the relic density increases until it reaches the opening of the W^+W^- annihilation channel and then decreases. It reaches the experimental value when the coannihilation with the lightest chargino $\tilde{\chi}_1^\pm$ (and marginally with $\tilde{\chi}_2^0$) becomes efficient enough. Since the field $\tilde{\chi}_1^\pm$ is dominantly Triplino (we are assuming $\mu \gg \mu_\Sigma$), the coannihilation cross section strictly depends on the tuning between μ_Σ and M_1 . In particular, the correct relic density occurs for $M_1 < \mu_\Sigma$ and the LSP is Bino-like (cf. right panel). Since in this region also the LUX constraint is fulfilled, it results that in the TMSSM a well-tempered Bino-Triplino neutralino can be a good DM candidate.

The behaviors of the relic density and SI cross section shown in the figure is then a proof of concept for the DM in the TMSSM. Indeed we find two qualitatively-different regions where the LSP satisfies the DM constraints. In the next two sections we discuss them in detail, still in the M_2 decoupling limit.

6.1 Well-tempered ‘Bino-Triplino’ neutralino

As it is well known, in MSSM scenarios with well-tempered neutralinos the correct relic density is achieved by a tuning of the Bino and Wino (or Higgsino) mass parameters to get an opportune balance between the large annihilation cross-sections of the Bino and the small ones of the Wino (or Higgsino) [25]. In the TMSSM with M_2 above the TeV scale, the role of the Wino is replaced by the Triplino, which still has gauge interactions with the W bosons. The channels contributing to the relic density are the chargino annihilation into W^+W^- , ZZ followed by the coannihilations $\tilde{\chi}_1^0 \tilde{\chi}_1^\pm \rightarrow ZW^\pm, q\bar{q}'$. The relevance of the

former processes with respect to the latter ones depends on the exact hierarchy between M_1 and μ_Σ . The μ parameter is instead constrained by LUX. Indeed, due to the LUX bound the Higgsino components of the LSP have to be small in order to suppress the $g_{h\tilde{\chi}_1^0\tilde{\chi}_1^0}$ coupling that is the main responsible for the SI cross section via Higgs exchange. This is illustrated in figure 6, where the SI cross section is plotted as a function of μ_Σ .

In all panels of the figure we fix $\tan\beta = 2.9$, $\lambda = 0.88$ and $M_2 = 1.5$ TeV. Besides the quantities shown in figure 5, also the values of $R_{\gamma\gamma}$ are displayed (for the color code of each quantity see the legend). At each point the parameter M_1 is adjusted just below μ_Σ to reproduce the observed relic density. For $\mu = 300$ GeV (top panels), the LSP is mostly Bino but the amount of its subdominant components vary at different μ_Σ . For light LSPs, the Triplino mixing is comparable to the Higgsino ones and the SI cross section is below the LUX limit. As soon as both Higgsino components reach the Triplino one, the SI cross-section is excluded by the LUX bound. By increasing μ to 500 GeV (bottom panels), the Higgsino mixings at a given μ_Σ become smaller than in the $\mu = 300$ GeV case, and the SI remains below the LUX bound in a wider range: $\tilde{\chi}_1^0$ satisfies all DM constraints in the mass range of $90\div 200$ GeV. The Higgsino components tend to be always larger than the Triplino one, as the Triplino connects with the Bino only via the Higgsino mixing (see eq. (3.3)). The figure confirms as well that the mechanism that provides the relic density is a balance between annihilation and coannihilation with the lightest chargino, as both particles are close in mass. The contribution of $\tilde{\chi}_2^0$ in coannihilation is marginal and depends strongly on the exact mixing.

Of course, the minimal μ value that LUX allows depends on the parameters that we have kept fixed in the figure. In particular, the LUX bound on μ becomes stronger at small $\tan\beta$ (see eq.(3.2)). This anti-correlation is discussed more in detail in section 6.4. However, we can anticipate that it affects negatively the enhancements of both $\gamma\gamma$ and $Z\gamma$ Higgs signals. Indeed, as previously discussed, large $R_{\gamma\gamma}$ and $R_{Z\gamma}$ require either $\tan\beta$ and μ to be small. This is confirmed by the brown line in the left panel of figure 6: for the considered parameter set, the maximal $R_{\gamma\gamma}$ drops as μ goes from 300 GeV to 500 GeV.

6.2 DM at the Higgs and Z resonances

The Higgs and Z boson resonances are fine-tuned regions as they rely on the fact that for $M_1 \sim m_h/2$ and $M_1 \sim m_Z/2$ the annihilation cross-section gets enhanced, hence decreasing the relic density. We first comment on the Higgs pole.

The case of the Higgs resonance is peculiar because the phenomenology of the LSP can be reconducted to one coupling only. The vertex Bino-Higgsino-Higgs is responsible for both the annihilation ($\tilde{\chi}_1^0\tilde{\chi}_1^0 \rightarrow h \rightarrow q\bar{q}$) and the SI scattering cross-section since the neutralino is mostly pure Bino. Hence the key parameters are M_1 and μ , whereas there is a minor dependence on both μ_Σ and M_2 . Similarly to the case of the well-tempered neutralino, the μ parameter is constrained by the LUX bound, as illustrated in figure 7 where at each point M_1 is tuned at the Higgs resonance to achieve the observed relic density. (The plotted quantities and their color code are as in figure 6). Indeed for $\mu = 300$ GeV (top panels), the SI cross-section is only marginally compatible with the LUX constraint at large μ_Σ and clearly a small decrease in μ will exclude these points (cf. top and bottom left

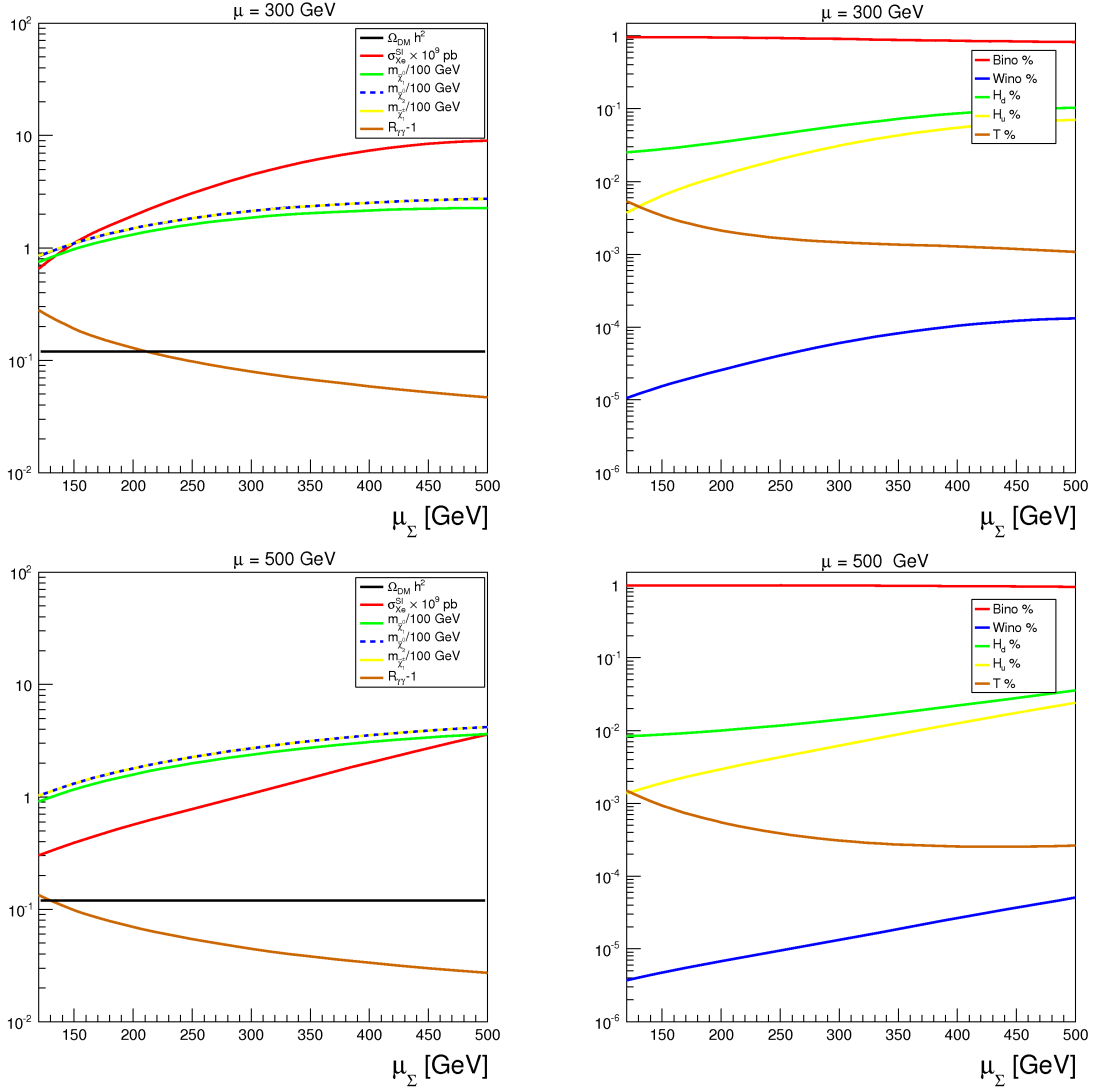


Figure 6. *Top left:* Dependence of $\sigma_{X_e}^{SI}$ (red line), $R_{\gamma\gamma} - 1$ (brown line), $m_{\tilde{\chi}_1^0}$ (green line), $m_{\tilde{\chi}_1^\pm}$ (yellow line) and $m_{\tilde{\chi}_2^0}$ (blue line) on μ_Σ . M_1 is adjusted to satisfy $\Omega_{\text{DM}}h^2 = 0.12$ (black solid line) for the well-tempered neutralino. The other parameters are $\mu = 300$ GeV, $\lambda = 0.88$, $\tan\beta = 2.9$ and $M_2 = 1.5$ TeV. *Top right:* LSP composition as a function of μ_Σ , as labelled in the caption. The other parameters are as in the left panel. *Bottom:* As above but for $\mu = 500$ GeV.

panels). The behavior of the SI cross-section is only mildly dependent on μ_Σ , as it is almost flat over all μ_Σ range. This is even more manifest for $\mu = 500$ GeV (lower panels). For such a μ value the SI cross section is well below the experimental bound. From the right panels it is clear that the LSP is almost pure Bino and that the dominant annihilation channels is a Higgs exchange on s -channel. Indeed, due to the large mass gap between the lightest neutralino and the other charginos and neutralinos (left panel), coannihilation is completely irrelevant.

In the Higgs resonance region one might expect to have large $R_{\gamma\gamma}$ and $R_{Z\gamma}$ signal

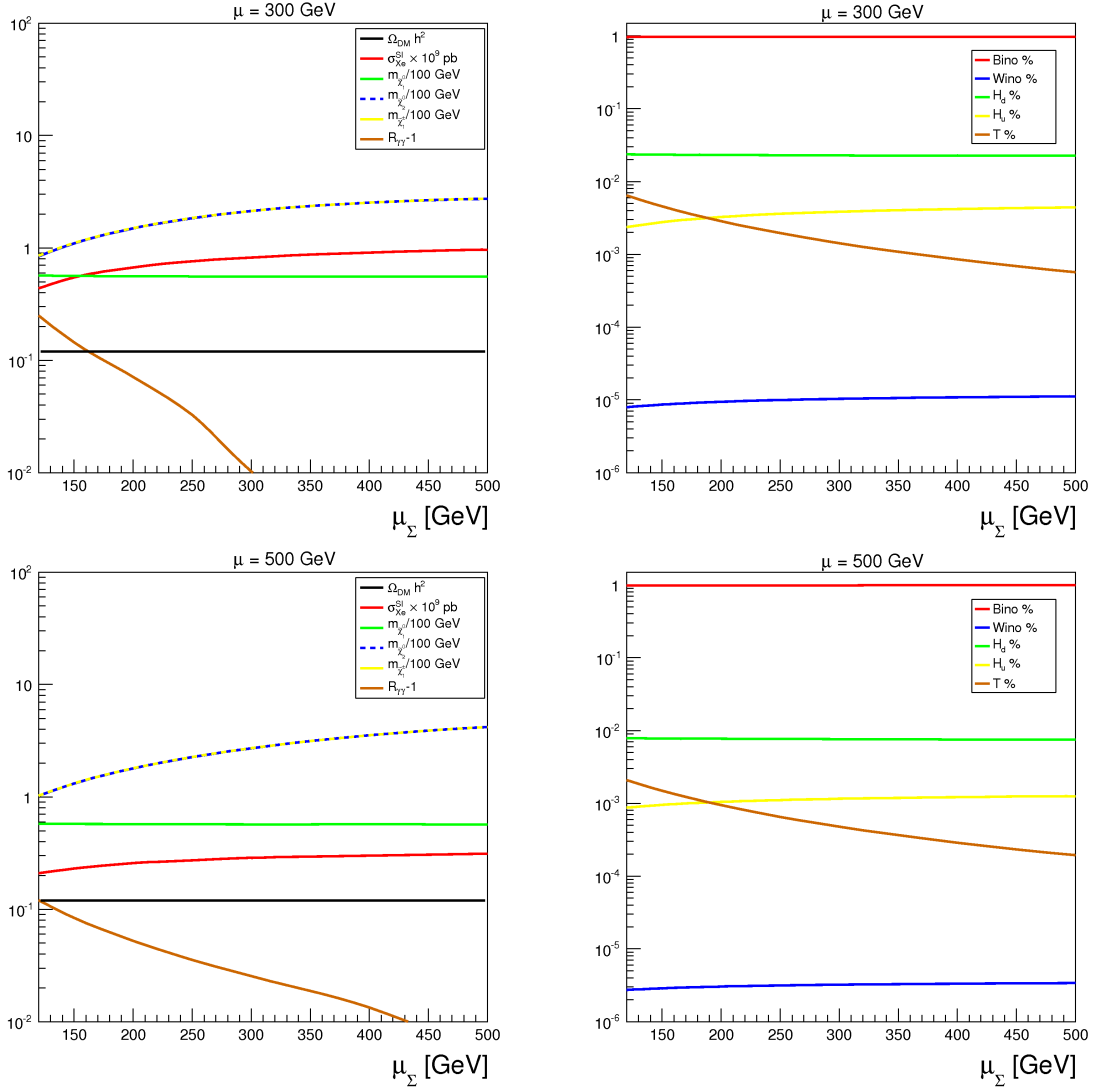


Figure 7. All panels: Same as figure 6 for the Higgs pole. M_1 is chosen to satisfy the relic density and to be $M_1 \simeq m_h/2$.

strengths because the DM phenomenology is not tightly bounded to the Triplino component. In other words the μ_Σ parameter is not correlated to $\sigma_{\text{Xe}}^{\text{SI}}$ or $\Omega_{\text{DM}} h^2$, and therefore can take low values such that the lightest chargino mass is close to the LEP bound. However, the anti-correlation between $\tan\beta$ and μ mentioned in section 6.1, is present in this region as well. Therefore, the enhancement in the $R_{\gamma\gamma}$ turns out to be at most $\sim 10\%$ for $\mu = 300$ GeV and negligible for $\mu = 500$ GeV, as indicated by the brown line in the left panel of figure 7. We will discuss this issue in detail in section 6.4.

A similar reasoning applies to the Z resonance region, with the difference that in that region the process that fixes the relic density, which is proportional to the Z -Higgsino coupling of the LSP (given in eq. (3.4)), is uncorrelated from the SI elastic cross-section.

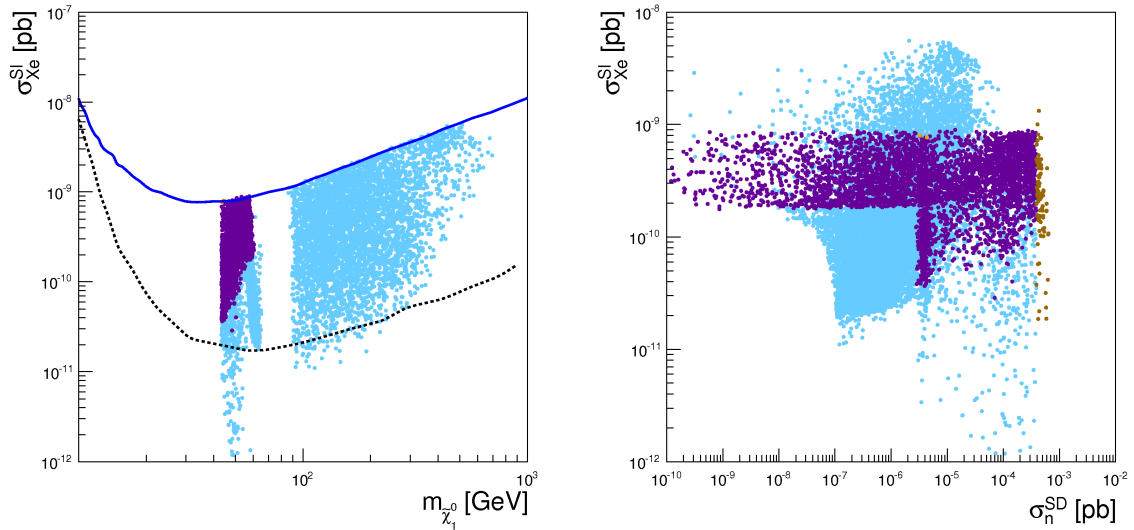


Figure 8. *Left:* Equal weight posterior sample in the $\{\sigma_{\text{Xe}}^{\text{SI}} - m_{\tilde{\chi}_1^0}\}$ -plane. The solid blue line stands for the LUX exclusion limit, while the black dotted line is the projected sensitivity of XENON1T. The color code is as in figure 4 and indicates the Higgs into invisible branching ratio percentage when the channel is open. *Right:* Same as left in the $\{\sigma_{\text{Xe}}^{\text{SI}} - \sigma_n^{\text{SD}}\}$ -plane. The brown points stand for points at odds with the XENON100 exclusion bound for σ_n^{SD} .

6.3 DM in the TMSSM: global survey

In this section we present the results of a comprehensive sampling of the TMSSM parameter space, using the likelihood $\mathcal{L}_{\text{DM}}(d|\theta_i)$ and the prior ranges described in section 4.

Figure 8 (left panel) shows the mass value for which the LSP is a viable DM candidate compatible with LUX (blue solid). As discussed above, there are two separate regions: one with the resonances at $40 \text{ GeV} \lesssim m_{\tilde{\chi}_1^0} \lesssim 70 \text{ GeV}$, and one with a well-tempered neutralino at $m_{\tilde{\chi}_1^0} \gtrsim 90 \text{ GeV}$. The apparent upper limit at about 600 GeV is an artifact of the prior range choice for the mass parameters. Notice that almost all the parameter space is in the sensitivity range of XENON1T [73] (black dotted line), so an effective TMSSM might be probed by DM direct searches in 5-7 years time¹¹. In our sample the minimal values of $\sigma_{\text{Xe}}^{\text{SI}}$ correspond to the contribution to the SI cross-section due to squarks exchange, when the Higgsino component start to be negligible. The value is similar in all the sample as the squark sector is kept heavy. More interestingly, the requirement of having the LSP as good DM candidate sets as well an upper bound on the Higgs invisible branching ratio $\text{BR}(h \rightarrow \tilde{\chi}_1^0 \tilde{\chi}_1^0) < 20\%$ (violet points), which is comparable to current LHC bounds [63–66] (indeed there are the very few dark yellow points with $\text{BR}(h \rightarrow \tilde{\chi}_1^0 \tilde{\chi}_1^0) > 20\%$). This illustrates the complementarity between DM direct searches and colliders: significant values of the Higgs invisible width can be fully probed by XENON1T.

In the right panel of figure 8 we show the $\sigma_{\text{Xe}}^{\text{SI}}$ versus the SD cross-section on neutron

¹¹However, we stress that the accuracy of the present analysis does not allow for refined comparison between the TMSSM and XENON1T. Indeed, our estimate of the SI cross section does not take into account loop-induced corrections of the order of $\mathcal{O}(10^{-11})$ pb [74].

(which is equivalent to the one on proton). As in the previous figures, violet points represent parameter configurations with $\text{BR}(h \rightarrow \tilde{\chi}_1^0 \tilde{\chi}_1^0) > 1\%$, whereas brown points correspond to SD cross-section values at odds with the XENON100 exclusion bound, whose strongest limit $\sigma_n^{\text{SD}} \lesssim 3 \times 10^{-4}$ pb is at $m_{\tilde{\chi}_1^0} \sim 50$ GeV. We do not remove the brown points from our samples as the nuclear uncertainties on the structure functions for the nucleons are large and can affect the predicted number of events by a factor of 3-4 [72, 75, 76]. In addition the predictions for the SD on proton give the same value, however these values are below the COUPP sensitivity, which reaches the maximum at $\sigma_p^{\text{SD}} \sim 5 \times 10^{-3}$ pb for $m_{\tilde{\chi}_1^0} \sim 40$ GeV. These points with large $\sigma_{p,n}^{\text{SD}}$ are associated to the t -channel Z boson exchange and arise when Higgsino components are sizable. They correspond to the Z resonance region, where the coupling $g_{Z\tilde{\chi}_1^0\tilde{\chi}_1^0}$ is large. In the case of SD scattering there is a one-to-one correspondence with the annihilation cross-section mediated by the Z boson. The main bulk of the sample is however below the current SD bounds, because the coupling to the Z boson tends to be suppressed for most of the LSP composition, being predominantly Bino-like. The sharp cut on the upper values of SD and SI when the Higgs channel into invisible is open is due to the LUX bounds. XENON1T will be less sensitive to SD interaction (perhaps $\sim 10^{-6}$ pb), hence the model is more likely to be tested with the SI cross-section and the brown points will all be probed, independently of the nuclear uncertainties.

When M_2 is decreased to the same scale as the other chargino parameters, the phenomenology of the DM is wider and the tight bound on the lower limit of μ described above (sections 6.1 and 6.2) is relaxed by the additional admixture with the Wino component. This is illustrated in figure 9, where we display the LSP mass versus the neutralino and chargino parameters as labelled. From the top left panel, it is clear that the LSP is mostly Bino, as $m_{\tilde{\chi}_1^0}$ and M_1 follow each other over all the allowed range. From the other three panels it is striking that the Higgs and Z resonances are mostly independent from M_2 and μ_Σ as they can acquire approximately any allowed value.

The case of the well-tempered neutralino, where all possible combinations of compositions for the are available, is more interesting. Indeed the LSP can be mixed Bino-Triplino, as discussed above, but it can never be Triplino dominated because the LSP would be the corresponding chargino. Successful DM candidates can also show up as MSSM-like states, that is Bino-Wino, in which case the relic density is achieved by neutralino annihilation into W^+W^- and coannihilation with the lightest chargino producing $q\bar{q}'$. These MSSM-like scenarios are however less appealing because the condition $M_1 \sim M_2$ is not recovered by the usual supersymmetry-breaking mechanisms. Of course, a large portion of the parameter space presents mixed Bino-Triplino-Wino LSP, for which the dominant annihilation and coannihilation channels are $\tilde{\chi}_1^0\tilde{\chi}_{1,2}^0 \rightarrow W^+W^-$ and $\tilde{\chi}_1^0\tilde{\chi}_1^\pm \rightarrow q\bar{q}'$. Due to the LUX bound only μ larger than about 300 GeV is allowed. Moreover, the relic density is achieved by a mixture of annihilation and coannihilation. More specifically the main processes are $\tilde{\chi}_1^0\tilde{\chi}_1^0 \rightarrow hZ, q\bar{q}$ and $\tilde{\chi}_1^0\tilde{\chi}_1^\pm \rightarrow ZW^\pm$. Instead, when all components (Bino-Triplino-Wino-Higgsino) in the LSP are sizable, the main annihilation channels are the following: $\tilde{\chi}_1^\pm\tilde{\chi}_1^\pm \rightarrow W^\pm W^\pm$, $\tilde{\chi}_1^0\tilde{\chi}_1^\pm \rightarrow hW^\pm$ and $\tilde{\chi}_1^0\tilde{\chi}_1^0 \rightarrow hZ$.

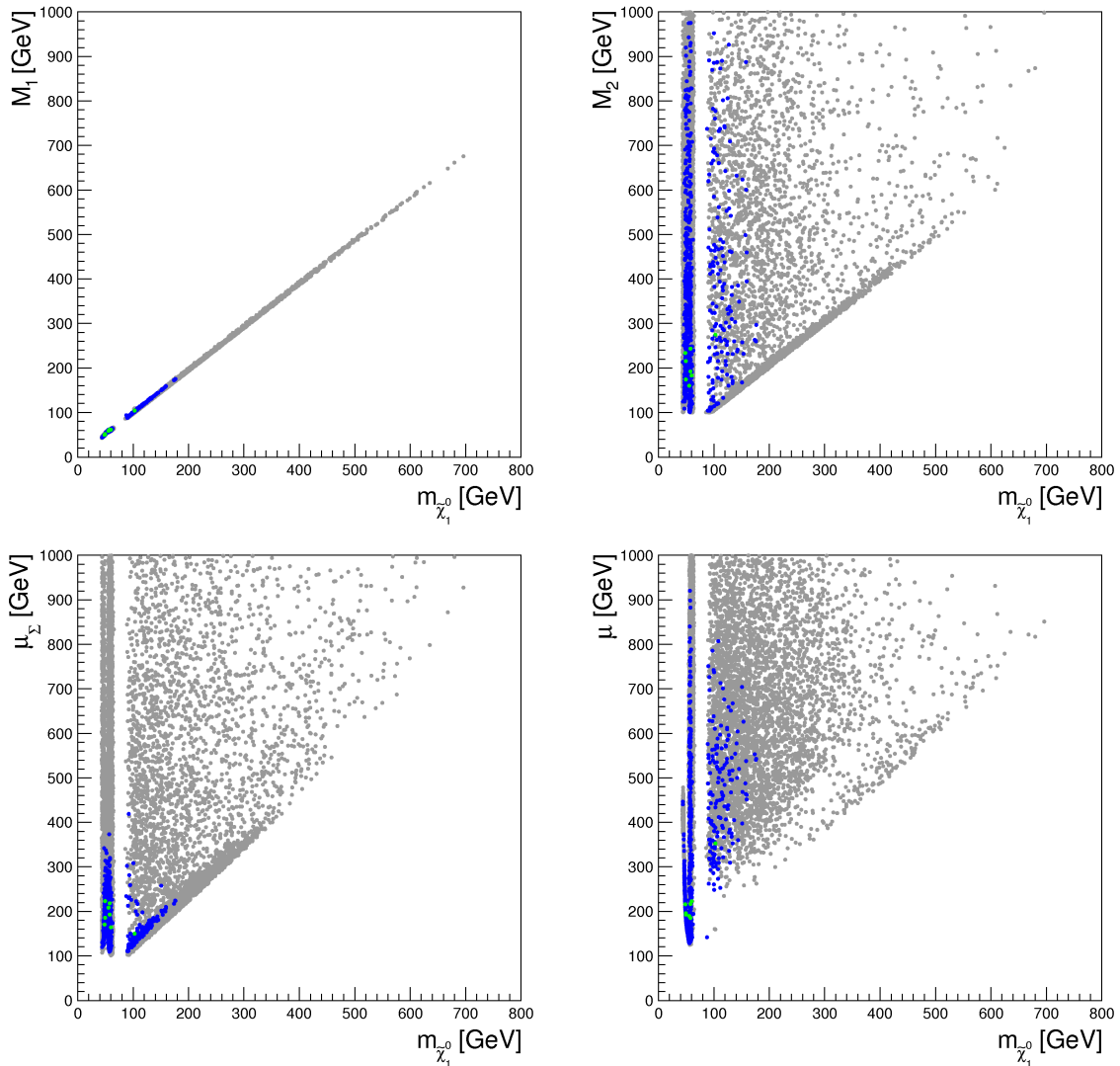


Figure 9. *Top left:* M_1 dependence of the mass of the LSP $m_{\tilde{\chi}_1^0}$. *Top right:* Same as left for M_2 . *Bottom:* Same as top left for μ_Σ and μ . The color code is as in figure 3.

6.4 DM implications on $R_{\gamma\gamma}$ and $R_{Z\gamma}$

Figure 10 shows the $\gamma\gamma$ signal strength versus the $Z\gamma$ one, similarly to figure 4. The possible $R_{\gamma\gamma}$ and $R_{Z\gamma}$ that can be achieved in the TMSSM where the DM constraints are satisfied, are displayed in cyan. They are superposed to the points of figure 4 where no DM observable is imposed (here displayed in green). The DM constraints alleviate the change in slope that arises in the correlation plot without DM constraints (cf. left panel of figure 4): the cyan points follow a smooth pattern with respect to the dark green ones. As previously discussed, the missing dark green zone in the upper part of that plot is due to a Higgs branching ratio varying very fast as soon as it is kinematically open. There, to get small reduction in the signal strength, M_1 should lie exactly on the threshold value, which is a very infrequent situation. On the contrary, with the LSP being DM, the relic

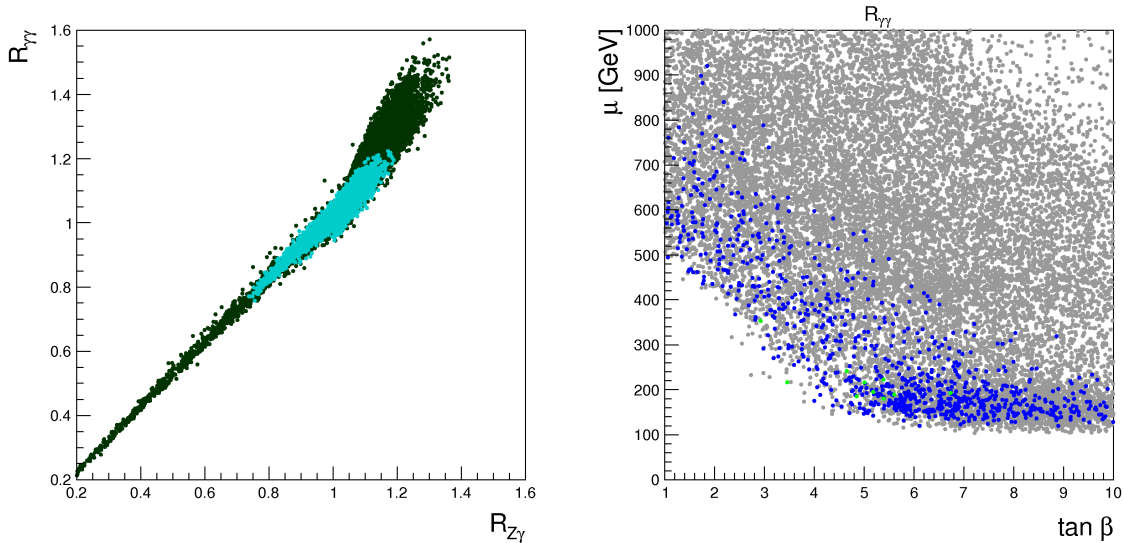


Figure 10. *Left:* Correlation between $R_{\gamma\gamma}$ and $R_{Z\gamma}$ for the equal weight posterior sample for the no DM case (green points) and for the DM case (cyan points). *Right:* Correlation between $\tan\beta$ and μ for the equal weight posterior sample for the DM case. Same color code as in figure 3.

density constraint requires $M_1 \sim m_{h,Z}/2$ (or the well-tempered neutralino conditions) and therefore a large portion of the sampled parameter space is concentrated in the pole regions.

On the other hand, on general basis, the DM constraints are not encouraging about the collider Higgs phenomenology. Indeed, our analysis leads to

$$R_{\gamma\gamma} \lesssim 1.25, \quad R_{Z\gamma} \lesssim 1.2 \quad (\text{with DM obs.}) . \quad (6.1)$$

The most stringent constraint on the parameter space where large $R_{\gamma\gamma}$ and $R_{Z\gamma}$ are achieved, is the LUX bound on SI cross-section, which rules out the configurations where either μ and $\tan\beta$ are simultaneously small: the anti-correlation between these two variables is striking from the right panel of figure 10¹². In particular, for $\tan\beta \simeq 1$ the LSP is a viable DM candidate only for $\mu > 500$ GeV, i.e. it is incompatible with the ballpark that provides the largest possible enhancements (see figure 4). The possibility of achieving sizeable loop-induced decays of the Higgs and at the same time a successful neutralino DM particle, starts arising at $\tan\beta \gtrsim 3$ and $\mu \gtrsim 300$ GeV: this is exactly the region that saturates the bounds in eq. (6.1), as shown by the green points in the right panel (these points have $R_{\gamma\gamma} > 20\%$). The mild enhancement of 10% is viable in all $\tan\beta$ range, as it is due to small values of μ_Σ . This is illustrated in figure 11. In the left panel we show the projection of the $R_{\gamma\gamma}$ values as a function of λ and $\tan\beta$: the range of the Triplino coupling λ that provides the enhancements is limited with respect to figure 4, being scattered at around $0.8 \div 0.9$. Signal strengths larger than one can only be achieved for small values of μ_Σ (central panel); they are however only marginally sensitive to M_2 . The same points are instead concentrated to both small values of μ and μ_Σ (right panel) and they mostly correspond to the Higgs and Z resonance regions. This is confirmed by looking at the

¹²This correlation is proper of the MSSM and has been noticed for instance in ref. [77].

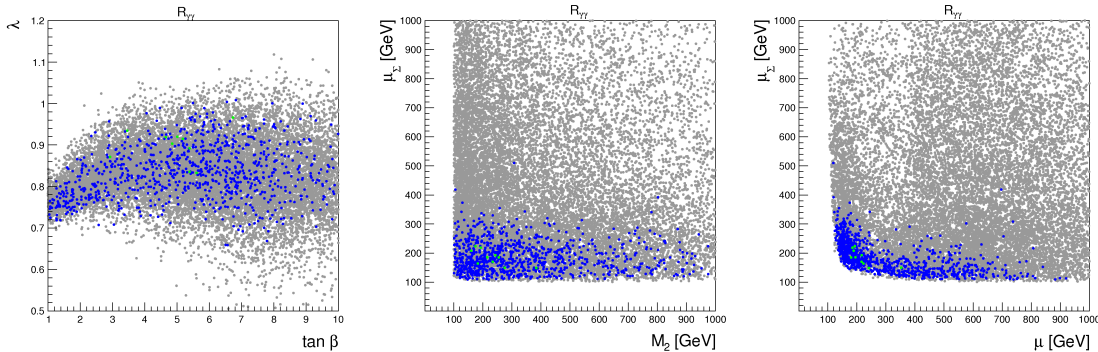


Figure 11. *Left:* $R_{\gamma\gamma}$ (third direction) projected in the $\{\lambda - \tan\beta\}$ -plane. Same color code as in figure 3. *Central and right:* Same as left in the $\{\mu_\Sigma - M_2\}$ and $\{\mu_\Sigma - \mu\}$ planes.

same sparse green/blue points in figure 9, which are mostly concentrated at values of $m_{\tilde{\chi}_1^0}$ around $40 \div 70$ GeV.

7 Conclusions

We are entering the era of precision Higgs physics: the measurements of the Higgs mass, couplings and decay modes have already started to be highly sensitive to new physics beyond the SM. In this paper we have considered the Higgs phenomenology of the $Y = 0$ triplet extension of the MSSM, dubbed TMSSM, in which the new coupling between the triplet and the MSSM Higgses can alleviate the little hierarchy problem and modify the chargino and neutralino sector.

We have first accurately determined the couplings and pole masses of the stops, charginos, neutralinos and lightest CP-even Higgs h . Then, we have tackled the subtle effects of the Triplino in the $h \rightarrow \gamma\gamma$ and $h \rightarrow Z\gamma$ loop-induced processes. We have shown that the additional Triplino component in the chargino sector provides a maximal enhancement of 60% in the $R_{\gamma\gamma}$ signal strength, which is slightly larger than previously estimated (i.e. $R_{\gamma\gamma} \lesssim 1.45$) [12]. An enhancement up to 40% can be achieved in the $R_{Z\gamma}$ signal strength, which we find to be highly correlated with the diphoton channel, even though it is always smaller than $R_{\gamma\gamma}$. The parameter region leading to the largest $R_{\gamma\gamma}$ and $R_{Z\gamma}$ is characterized by $\tan\beta \lesssim 2$ and $\mu \sim \mu_\Sigma \sim M_2 \sim 250$ GeV, and in particular by light charginos close to the LEP bound. The enhancement in the TMSSM is significantly larger than the one achievable in the MSSM ($\sim 20\%$ for $R_{\gamma\gamma}$) for the same chargino lower mass bound [16]. The measurements of these processes are likely to improve in the next years. LHC is indeed expected to probe the SM prediction of $\Gamma(h \rightarrow Z\gamma)$ once $\mathcal{O}(100 \text{ fb}^{-1})$ data is collected [78], and to measure the $g_{h\gamma\gamma}$ effective coupling within a 10% accuracy after a high luminosity 3000 fb^{-1} run [79]. With these further data the Higgs diphoton signal strength will plausibly converge to the SM value. In such a case, sizeable deviations in $h \rightarrow Z\gamma$ would not be compatible with the TMSSM. On the contrary, if data will still exhibit a positive deviation from the SM, there would be a clear indication of physics beyond

the SM. The above predictions and the tight correlation between $R_{\gamma\gamma}$ and $R_{Z\gamma}$ could be thus crucial to rule out or provide hints for the scenario considered here.

Besides the Higgs decays, we have investigated the DM phenomenology in the TMSSM, focusing on the interplay of the neutralino and chargino sectors enlarged by the triplet components. Similarly to the MSSM, the LSP is a viable DM candidate in the Higgs or Z pole region, and in the so-called well-tempered regime. The Higgs and Z pole regions are characterized by a Bino DM and are poorly sensitive to the Triplino, as the Higgs-Higgsino-Bino is the only relevant coupling. However, the well-tempered neutralino, where the LSP achieves the correct relic density via coannihilation with the lightest chargino, presents a new feature. Indeed the Triplino component of the LSP can substitute the Wino in the well-tempered neutralino and can solve the problem of having $M_1 \sim M_2$ from grand unified model perspective. Indeed the requirement of DM comes at the expenses of satisfying the LUX exclusion limit for SI elastic cross-section on nuclei. The dominant contribution is due to Higgs exchange, which imposes a lower bound on μ . Interestingly we found that this has an impact for the $R_{\gamma\gamma}$ and $R_{Z\gamma}$ enhancements: the Higgs-chargino coupling is reduced as well suppressing the signal strengths to at most 20%. Notice that these values are once again larger than the ones provided by the MSSM with DM constraints [16], when the Higgs production is SM-like.

The scenario considered here nicely illustrates the complementarity of DM direct searches with LHC. For instance the next generation of direct detection experiments, such as XENON1T, will probe a consistent portion of the neutralino TMSSM parameter space. Moreover it will be capable of constraining the Higgs invisible decay branching ratio up to 1%, in a time scale comparable to the LHC one. In general the TMSSM is less constrained by current LHC bounds on simplified models or supersymmetric searches. Indeed the presence of the Triplino can modify the couplings and the decay modes. This has been already observed for stops in the TMSSM [80] even though a precise estimate of their current mass bound is still missing. On the other hand no study exists for the chargino and neutralino mass bounds. Although we have checked that the present constraints [67, 68] do not apply to our analysis ballpark, a dedicated investigation would be required in order to accurately determine the allowed parameter region. Present data should primarily affect the chargino parameter region with light lightest-neutralino and with small $h \rightarrow Z\gamma$ and $h \rightarrow \gamma\gamma$ enhancements. With more LHC data strongest bounds are expected, in particular for the DM mass close to the Z or h resonance. On the other hand, in order to probe the coannihilation region (where the spectrum is compressed), ILC data and analyses similar to that proposed in ref. [81] would be crucial.

Acknowledgments

We are very grateful to Florian Staub for useful explanations about `SPheno` and `SARAH` programs. We also thank the authors of `CPsuperH`, in particular Jae Sik Lee, for their help in numerical issues. GN thanks A. Delgado and M. Quiros for useful discussions. CA acknowledges the support of the ERC project 267117 (DARK) hosted by Université Pierre et Marie Curie - Paris 6, PI J. Silk. GN was supported by the German Science Foundation

(DFG) within the Collaborative Research Center 676 “Particles, Strings and Early Universe”. VML acknowledges the support of the Consolider-Ingenio 2010 programme under grant MULTIDARK CSD2009-00064, the Spanish MICINN under Grant No. FPA2012-34694, the Spanish MINECO Centro de excelencia Severo Ochoa Program under Grant No. SEV-2012-0249, and the European Union under the ERC Advanced Grant SPLE under contract ERC-2012-ADG-20120216-320421.

References

- [1] **CMS** Collaboration, *Combination of standard model Higgs boson searches and measurements of the properties of the new boson with a mass near 125 GeV*, Tech. Rep. CMS-PAS-HIG-13-005, 2013.
- [2] **ATLAS** Collaboration, *Combined coupling measurements of the Higgs-like boson with the ATLAS detector using up to 25 fb⁻¹ of proton-proton collision data*, Tech. Rep. ATLAS-CONF-2013-034, ATLAS-COM-CONF-2013-035, 2013.
- [3] J. Espinosa and M. Quiros, *Upper bounds on the lightest Higgs boson mass in general supersymmetric Standard Models*, *Phys.Lett.* **B302** (1993) 51–58, [[hep-ph/9212305](#)].
- [4] A. Arbey, M. Battaglia, A. Djouadi, F. Mahmoudi, and J. Quevillon, *Implications of a 125 GeV Higgs for supersymmetric models*, *Phys.Lett.* **B708** (2012) 162–169, [[arXiv:1112.3028](#)].
- [5] M. Carena, S. Gori, N. R. Shah, and C. E. Wagner, *A 125 GeV SM-like Higgs in the MSSM and the $\gamma\gamma$ rate*, *JHEP* **1203** (2012) 014, [[arXiv:1112.3336](#)].
- [6] Z. Kang, T. Li, J. Li, and Y. Liu, *A Radiatively Light Stop Saves the Best Global Fit for Higgs Boson Mass and Decays*, [arXiv:1208.2673](#).
- [7] J. Fan and M. Reece, *A New Look at Higgs Constraints on Stops*, [arXiv:1401.7671](#).
- [8] J. Espinosa and M. Quiros, *Higgs triplets in the supersymmetric standard model*, *Nucl.Phys.* **B384** (1992) 113–146.
- [9] U. Ellwanger, C. Hugonie, and A. M. Teixeira, *The Next-to-Minimal Supersymmetric Standard Model*, *Phys.Rept.* **496** (2010) 1–77, [[arXiv:0910.1785](#)].
- [10] **ATLAS** Collaboration, G. Aad et al., *Observation of a new particle in the search for the Standard Model Higgs boson with the ATLAS detector at the LHC*, *Phys.Lett.* **B716** (2012) 1–29, [[arXiv:1207.7214](#)].
- [11] **CMS** Collaboration, S. Chatrchyan et al., *Observation of a new boson at a mass of 125 GeV with the CMS experiment at the LHC*, *Phys.Lett.* **B716** (2012) 30–61, [[arXiv:1207.7235](#)].
- [12] A. Delgado, G. Nardini, and M. Quiros, *Large diphoton Higgs rates from supersymmetric triplets*, *Phys.Rev.* **D86** (2012) 115010, [[arXiv:1207.6596](#)].
- [13] Z. Kang, Y. Liu, and G.-Z. Ning, *Highlights of Supersymmetric Hypercharge ± 1 Triplets*, *JHEP* **1309** (2013) 091, [[arXiv:1301.2204](#)].
- [14] T. Basak and S. Mohanty, *130 GeV gamma ray line and enhanced Higgs di-photon rate from Triplet-Singlet extended MSSM*, [arXiv:1304.6856](#).
- [15] B. Batell, S. Jung, and C. E. Wagner, *Very Light Charginos and Higgs Decays*, *JHEP* **1312** (2013) 075, [[arXiv:1309.2297](#)].

- [16] J. A. Casas, J. M. Moreno, K. Rolbiecki, and B. Zaldivar, *Implications of light charginos for Higgs observables, LHC searches and dark matter*, [arXiv:1305.3274](#).
- [17] G. Belanger, V. Bizouard, and G. Chalons, *Boosting Higgs decays into gamma and a Z in the NMSSM*, [arXiv:1402.3522](#).
- [18] A. Delgado, G. Nardini, and M. Quiros, *A Light Supersymmetric Higgs Sector Hidden by a Standard Model-like Higgs*, *JHEP* **1307** (2013) 054, [[arXiv:1303.0800](#)].
- [19] J. Cao, L. Wu, P. Wu, and J. M. Yang, *The Z+photon and diphoton decays of the Higgs boson as a joint probe of low energy SUSY models*, *JHEP* **1309** (2013) 043, [[arXiv:1301.4641](#)].
- [20] L. Covi, J. E. Kim, and L. Roszkowski, *Axinos as cold dark matter*, *Phys.Rev.Lett.* **82** (1999) 4180–4183, [[hep-ph/9905212](#)].
- [21] H. Baer, M. Haider, S. Kraml, S. Sekmen, and H. Summy, *Cosmological consequences of Yukawa-unified SUSY with mixed axion/axino cold and warm dark matter*, *JCAP* **0902** (2009) 002, [[arXiv:0812.2693](#)].
- [22] F. D. Steffen, *Dark Matter Candidates - Axions, Neutralinos, Gravitinos, and Axinos*, *Eur.Phys.J.* **C59** (2009) 557–588, [[arXiv:0811.3347](#)].
- [23] J. L. Feng, *Dark Matter Candidates from Particle Physics and Methods of Detection*, *Ann.Rev.Astron.Astrophys.* **48** (2010) 495–545, [[arXiv:1003.0904](#)].
- [24] G. Gelmini and P. Gondolo, *DM Production Mechanisms*, [arXiv:1009.3690](#).
- [25] N. Arkani-Hamed, A. Delgado, and G. Giudice, *The Well-tempered neutralino*, *Nucl.Phys.* **B741** (2006) 108–130, [[hep-ph/0601041](#)].
- [26] **LUX** Collaboration, D. Akerib et al., *First results from the LUX dark matter experiment at the Sanford Underground Research Facility*, [arXiv:1310.8214](#).
- [27] S. Di Chiara and K. Hsieh, *Triplet Extended Supersymmetric Standard Model*, *Phys.Rev.* **D78** (2008) 055016, [[arXiv:0805.2623](#)].
- [28] **Particle Data Group** Collaboration, J. Beringer et al., *Review of Particle Physics (RPP)*, *Phys.Rev.* **D86** (2012) 010001.
- [29] **ATLAS** Collaboration, G. Aad et al., *Search for third generation scalar leptoquarks in pp collisions at $\sqrt{s} = 7$ TeV with the ATLAS detector*, *JHEP* **1306** (2013) 033, [[arXiv:1303.0526](#)].
- [30] **CMS** Collaboration, S. Chatrchyan et al., *Search for top-squark pair production in the single-lepton final state in pp collisions at $\sqrt{s} = 8$ TeV*, tech. rep., 2013.
- [31] **CMS** Collaboration, S. Chatrchyan et al., *Search for gluino mediated bottom- and top-squark production in multijet final states in pp collisions at 8 TeV*, *Phys.Lett.* **B725** (2013) 243–270, [[arXiv:1305.2390](#)].
- [32] **ATLAS** Collaboration, “Gluino-mediated stop production.” https://atlas.web.cern.ch/Atlas/GROUPS/PHYSICS/CombinedSummaryPlots/SUSY/index.html#ATLAS_SUSY_Gtt, 2013.
- [33] R. Franceschini and R. Torre, *RPV stops bump off the background*, *Eur.Phys.J.* **C73** (2013) 2422, [[arXiv:1212.3622](#)].
- [34] B. Fuks and G. Nardini, “Light stops.” work in preparation.
- [35] M. Papucci, J. T. Ruderman, and A. Weiler, *Natural SUSY Endures*, *JHEP* **1209** (2012) 035, [[arXiv:1110.6926](#)].

- [36] **ATLAS** Collaboration, *Combined measurements of the mass and signal strength of the Higgs-like boson with the ATLAS detector using up to 25 fb⁻¹ of proton-proton collision data*, tech. rep., 2013.
- [37] P. Bandyopadhyay, K. Huitu, and A. Sabanci, *Status of $Y = 0$ Triplet Higgs with supersymmetry in the light of ~ 125 GeV Higgs discovery*, [arXiv:1306.4530](#).
- [38] F. Staub, *From Superpotential to Model Files for FeynArts and CalcHep/CompHep*, *Comput.Phys.Commun.* **181** (2010) 1077–1086, [[arXiv:0909.2863](#)].
- [39] F. Staub, *Automatic Calculation of supersymmetric Renormalization Group Equations and Self Energies*, *Comput.Phys.Commun.* **182** (2011) 808–833, [[arXiv:1002.0840](#)].
- [40] W. Porod, *SPheno, a program for calculating supersymmetric spectra, SUSY particle decays and SUSY particle production at e^+e^- colliders*, *Comput.Phys.Commun.* **153** (2003) 275–315, [[hep-ph/0301101](#)].
- [41] W. Porod and F. Staub, *SPheno 3.1: Extensions including flavour, CP-phases and models beyond the MSSM*, *Comput.Phys.Commun.* **183** (2012) 2458–2469, [[arXiv:1104.1573](#)].
- [42] B. Allanach, A. Djouadi, J. Kneur, W. Porod, and P. Slavich, *Precise determination of the neutral Higgs boson masses in the MSSM*, *JHEP* **0409** (2004) 044, [[hep-ph/0406166](#)].
- [43] **ATLAS** Collaboration, G. Aad et al., *Search for Invisible Decays of a Higgs Boson Produced in Association with a Z Boson in ATLAS*, [arXiv:1402.3244](#).
- [44] **CMS** Collaboration, CMS, *Search for invisible Higgs produced in association with a Z boson*, tech. rep., 2013.
- [45] **ALEPH, DELPHI, L3, OPAL, SLD, LEP Electroweak Working Group, SLD Electroweak Group, SLD Heavy Flavour Group** Collaboration, S. Schael et al., *Precision electroweak measurements on the Z resonance*, *Phys.Rept.* **427** (2006) 257–454, [[hep-ex/0509008](#)].
- [46] A. Djouadi, *The Anatomy of electro-weak symmetry breaking. II. The Higgs bosons in the minimal supersymmetric model*, *Phys.Rept.* **459** (2008) 1–241, [[hep-ph/0503173](#)].
- [47] **ATLAS** Collaboration, *Search for the Standard Model Higgs boson in the $H \rightarrow Z\gamma$ decay mode with pp collisions at $\sqrt{s} = 7$ and 8 TeV*, tech. rep., 2013.
- [48] **CMS** Collaboration, S. Chatrchyan et al., *Search for a Higgs boson decaying into a Z and a photon in pp collisions at $\sqrt{s} = 7$ and 8 TeV*, *Phys.Lett.* **B726** (2013) 587–609, [[arXiv:1307.5515](#)].
- [49] R. Cahn, M. S. Chanowitz, and N. Fleishon, *Higgs Particle Production by $Z \rightarrow H\gamma$* , *Phys.Lett.* **B82** (1979) 113.
- [50] L. Bergstrom and G. Hulth, *Induced Higgs Couplings to Neutral Bosons in e^+e^- Collisions*, *Nucl.Phys.* **B259** (1985) 137.
- [51] A. Djouadi, V. Driesen, W. Hollik, and A. Kraft, *The Higgs photon - Z boson coupling revisited*, *Eur.Phys.J.* **C1** (1998) 163–175, [[hep-ph/9701342](#)].
- [52] **Planck** Collaboration, P. Ade et al., *Planck 2013 results. XVI. Cosmological parameters.*, [arXiv:1303.5076](#).
- [53] F. Boudjema, G. Drieu La Rochelle, and S. Kulkarni, *One-loop corrections, uncertainties and approximations in neutralino annihilations: Examples*, *Phys.Rev.* **D84** (2011) 116001, [[arXiv:1108.4291](#)].

- [54] P. Junnarkar and A. Walker-Loud, *The Scalar Strange Content of the Nucleon from Lattice QCD*, *Phys.Rev.* **D87** (2013) 114510, [[arXiv:1301.1114](#)].
- [55] R. Koch, *A New Determination of the πN Sigma Term Using Hyperbolic Dispersion Relations in the (ν^{*2}, t) Plane*, *Z. Phys.* **C15** (1982) 161–168.
- [56] J. Gasser, H. Leutwyler, and M. E. Sainio, *Form-factor of the sigma term*, *Phys. Lett.* **B253** (1991) 260–264.
- [57] A. Bottino, F. Donato, N. Fornengo, and S. Scopel, *Implications for relic neutralinos of the theoretical uncertainties in the neutralino nucleon cross-section*, *Astropart. Phys.* **13** (2000) 215–225, [[hep-ph/9909228](#)].
- [58] M. M. Pavan, I. I. Strakovsky, R. L. Workman, and R. A. Arndt, *The pion nucleon Sigma term is definitely large: Results from a GWU analysis of πN scattering data*, *PiN Newslett.* **16** (2002) 110–115, [[hep-ph/0111066](#)].
- [59] R. R. de Austri and C. P. d. l. Heros, *Impact of nucleon matrix element uncertainties on the interpretation of direct and indirect dark matter search results*, [arXiv:1307.6668](#).
- [60] J. Lee, M. Carena, J. Ellis, A. Pilaftsis, and C. Wagner, *CPsuperH2.3: an Updated Tool for Phenomenology in the MSSM with Explicit CP Violation*, *Comput.Phys.Commun.* **184** (2013) 1220–1233, [[arXiv:1208.2212](#)].
- [61] G. Belanger, F. Boudjema, A. Pukhov, and A. Semenov, *micrOMEGAs3.1 : a program for calculating dark matter observables*, [arXiv:1305.0237](#).
- [62] F. Feroz, M. Hobson, and M. Bridges, *MultiNest: an efficient and robust Bayesian inference tool for cosmology and particle physics*, *Mon.Not.Roy.Astron.Soc.* **398** (2009) 1601–1614, [[arXiv:0809.3437](#)].
- [63] J. R. Espinosa, M. Muhlleitner, C. Grojean, and M. Trott, *Probing for Invisible Higgs Decays with Global Fits*, *JHEP* **1209** (2012) 126, [[arXiv:1205.6790](#)].
- [64] G. Belanger, B. Dumont, U. Ellwanger, J. Gunion, and S. Kraml, *Status of invisible Higgs decays*, *Phys.Lett.* **B723** (2013) 340–347, [[arXiv:1302.5694](#)].
- [65] P. P. Giardino, K. Kannike, I. Masina, M. Raidal, and A. Strumia, *The universal Higgs fit*, [arXiv:1303.3570](#).
- [66] J. Ellis and T. You, *Updated Global Analysis of Higgs Couplings*, *JHEP* **1306** (2013) 103, [[arXiv:1303.3879](#)].
- [67] **ATLAS Collaboration** Collaboration, G. Aad et al., *Search for direct production of charginos and neutralinos in events with three leptons and missing transverse momentum in $\sqrt{s} = 8\text{TeV}$ pp collisions with the ATLAS detector*, *JHEP* **1404** (2014) 169, [[arXiv:1402.7029](#)].
- [68] **CMS Collaboration** Collaboration, V. Khachatryan et al., *Searches for electroweak production of charginos, neutralinos, and sleptons decaying to leptons and W , Z , and Higgs bosons in pp collisions at 8 TeV*, [arXiv:1405.7570](#).
- [69] **LHCb Collaboration**, R. Aaij et al., *First Evidence for the Decay $B_s^0 \rightarrow \mu^+ \mu^-$* , *Phys.Rev.Lett.* **110** (2013) 021801, [[arXiv:1211.2674](#)].
- [70] **Heavy Flavor Averaging Group** Collaboration, Y. Amhis et al., *Averages of B -Hadron, C -Hadron, and tau-lepton properties as of early 2012*, [arXiv:1207.1158](#).

- [71] **COUPP** Collaboration, E. Behnke et al., *First Dark Matter Search Results from a 4-kg CF₃I Bubble Chamber Operated in a Deep Underground Site*, *Phys.Rev.* **D86** (2012) 052001, [[arXiv:1204.3094](#)].
- [72] **XENON100** Collaboration, E. Aprile et al., *Limits on spin-dependent WIMP-nucleon cross sections from 225 live days of XENON100 data*, *Phys.Rev.Lett.* **111** (2013) 021301, [[arXiv:1301.6620](#)].
- [73] **XENON1T** Collaboration, E. Aprile, *The XENON1T Dark Matter Search Experiment*, [arXiv:1206.6288](#).
- [74] M. Cirelli, N. Fornengo, and A. Strumia, *Minimal dark matter*, *Nucl.Phys.* **B753** (2006) 178–194, [[hep-ph/0512090](#)].
- [75] D. Cerdeno, M. Fornasa, J. Huh, and M. Peiro, *Nuclear uncertainties in the spin-dependent structure functions for direct dark matter detection*, *Phys.Rev.* **D87** (2013) 023512, [[arXiv:1208.6426](#)].
- [76] C. Arina, G. Bertone, and H. Silverwood, *Complementarity of direct and indirect Dark Matter detection experiments*, *Phys.Rev.* **D88** (2013) 013002, [[arXiv:1304.5119](#)].
- [77] M. Farina, M. Kadastik, D. Pappadopulo, J. Pata, M. Raidal, et al., *Implications of XENON100 and LHC results for Dark Matter models*, *Nucl.Phys.* **B853** (2011) 607–624, [[arXiv:1104.3572](#)].
- [78] J. M. Campbell, R. K. Ellis, W. T. Giele, and C. Williams, *Finding the Higgs boson in decays to $Z\gamma$ using the matrix element method at Next-to-Leading Order*, *Phys.Rev.* **D87** (2013), no. 7 073005, [[arXiv:1301.7086](#)].
- [79] M. E. Peskin, *Comparison of LHC and ILC Capabilities for Higgs Boson Coupling Measurements*, [arXiv:1207.2516](#).
- [80] J. de Blas, A. Delgado, B. Ostdiek, and M. Quirs, *Indirect effects of supersymmetric triplets in stop decays*, *JHEP* **1401** (2014) 177, [[arXiv:1311.3654](#)].
- [81] S. Porto, G. A. Moortgat-Pick, and K. Rolbiecki, *Towards discrimination of MSSM and NMSSM scenarios at colliders*, [arXiv:1404.1053](#).